

A Quartz-bearing Orthopyroxene-rich Websterite Xenolith from the Pannonian Basin, Western Hungary: Evidence for Release of Quartz-saturated Melts from a Subducted Slab

**E. BALI^{1*}, Z. ZAJACZ^{1,2}, I. KOVÁCS^{1,3}, CS. SZABÓ¹, W. HALTER²,
O. VASELLI⁴, K. TÖRÖK^{1,5} AND R. J. BODNAR⁶**

¹LITHOSPHERE FLUID RESEARCH LAB, DEPARTMENT OF PETROLOGY & GEOCHEMISTRY, INSTITUTE OF GEOGRAPHY AND EARTH SCIENCES, EÖTVÖS UNIVERSITY BUDAPEST (ELTE), PAZMANY SETANY 1/c, BUDAPEST, H-1117, HUNGARY

²INSTITUTE OF ISOTOPE GEOCHEMISTRY AND MINERAL RESOURCES, ETH ZÜRICH, SONNEGSTRASSE 5, ETH ZENTRUM, 8092 ZÜRICH, SWITZERLAND

³RESEARCH SCHOOL OF EARTH SCIENCES, BUILDING 61 MILLS ROAD, THE AUSTRALIAN NATIONAL UNIVERSITY, CANBERRA, ACT 0200, AUSTRALIA

⁴DEPARTMENT OF EARTH SCIENCES, UNIVERSITY OF FLORENCE, VIA G. LA PIRA, 4, FLORENCE, 50121, ITALY

⁵EÖTVÖS LORÁND GEOPHYSICAL INSTITUTE OF HUNGARY, BUDAPEST, COLUMBUS U. 17–23, H-1145, HUNGARY

⁶DEPARTMENT OF GEOSCIENCES, VIRGINIA TECH, BLACKSBURG, VA 24061, USA

**RECEIVED JANUARY 31, 2007; ACCEPTED DECEMBER 19, 2007
ADVANCE ACCESS PUBLICATION JANUARY 19, 2008**

An unusual quartz-bearing orthopyroxene-rich websterite xenolith has been found in an alkali basaltic tuff at Szigliget, Bakony–Balaton Highland Volcanic Field (BBHVF), western Hungary. Ortho- and clinopyroxenes are enriched in light rare earth elements (LREE), middle REE and Ni, and depleted in Nb, Ta, Sr and Ti compared with ortho- and clinopyroxenes occurring in either peridotite or lower crustal granulite xenoliths from the BBHVF. Both ortho- and clinopyroxenes in the xenolith contain primary and secondary silicate melt inclusions, and needle-shaped or rounded quartz inclusions. The melt inclusions are rich in SiO₂ and alkalis and poor in MgO, FeO and CaO. They are strongly enriched in LREE and large ion lithophile elements, and display negative Nb, Ta and Sr anomalies, and slightly positive Pb anomalies. The xenolith is interpreted to represent a fragment of an orthopyroxene-rich body that crystallized in the upper mantle from a hybrid melt that formed by interaction of mantle peridotite with a quartz-saturated silicate melt that was released from a subducted oceanic slab. Although the exact composition of the slab melt cannot be determined,

model calculations on major and trace elements suggest involvement of a metasedimentary component.

KEY WORDS: quartz; mantle; silicate melt inclusion; SiO₂-rich melt; subduction; Carpathian-Pannonian Region

INTRODUCTION AND GEOLOGICAL BACKGROUND

This paper describes a quartz-bearing orthopyroxene-rich websterite xenolith (sample Szg-klm01) found in alkali basaltic tuff at Szigliget [part of the Bakony–Balaton Highland Volcanic Field (BBHVF)] in western Hungary. To our knowledge, such quartz-bearing mantle xenoliths have not been described in the literature, although opx-rich olivine websterites have been reported from the

*Corresponding author. Present address: Bayerisches Geoinstitut, Universität Bayreuth, Universitätsstraße 30, D-95447 Bayreuth, Germany. Telephone: +49 (0)921 155-3729. Fax: +49 (0)921 55-3769. E-mail: Eniko.Bali@uni-bayreuth.de

© The Author 2008. Published by Oxford University Press. All rights reserved. For Permissions, please e-mail: journals.permissions@oxfordjournals.org

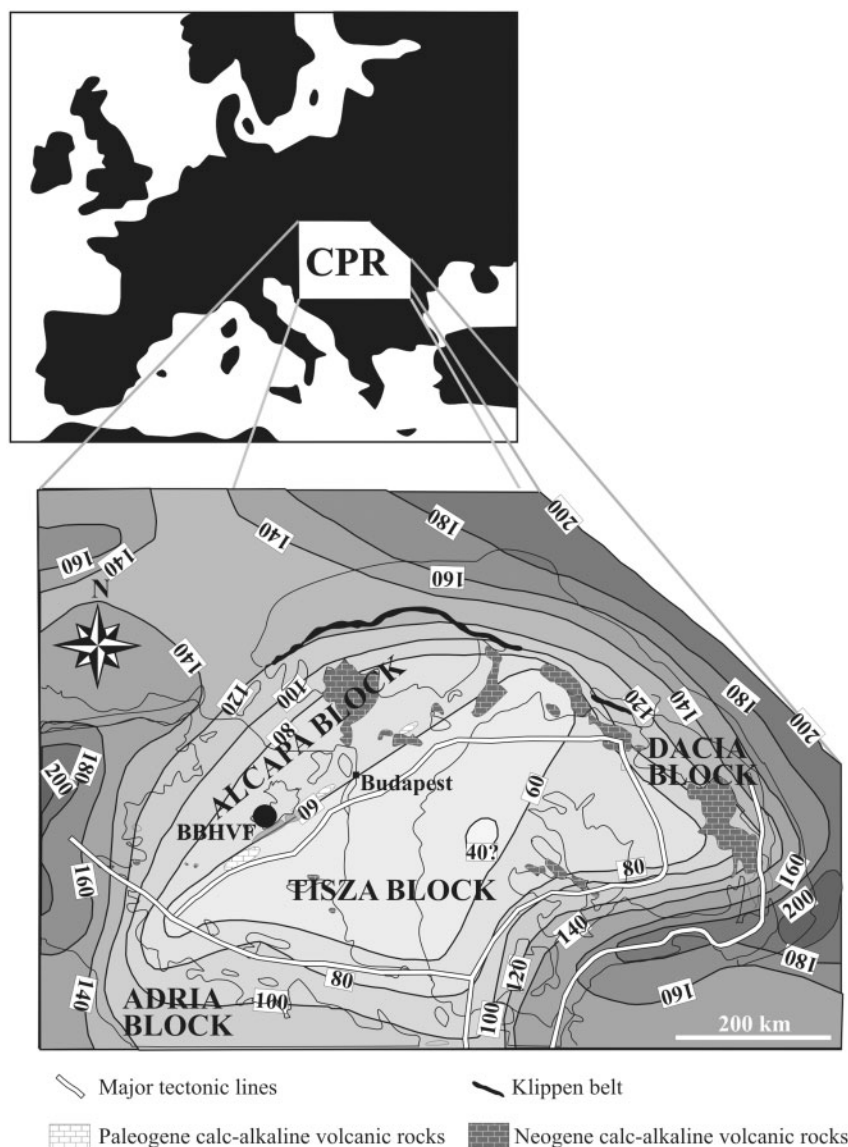


Fig. 1. Location map (top) showing the Carpathian–Pannonian Region (CPR) and a schematic geological map (bottom) of the CPR showing the lithosphere thickness (in km) beneath the region after Lenkey (1999), the location of Neogene and Paleogene calc-alkaline volcanic formations, and the location of the Bakony–Balaton Highland Volcanic Field (BBHVF). The Klippen belt is the proposed Neogene suture zone.

ultramafic xenolith suite of the BBHVF (Bali *et al.*, 2007). Both orthopyroxene (opx) and clinopyroxene (cpx) from the xenolith contain abundant primary and secondary silicate melt inclusions (MI). The major and trace element compositions of minerals and MI suggest that this rock is a fragment of a reaction zone between a slab-derived melt and mantle peridotite.

The BBHVF is located in the northern Carpathian–Pannonian Region (CPR) (Fig. 1) on the ALCAPA (ALpine–CArpathian–PAnnonian) basement mega-unit, which was transported *c.* 450 km eastwards from the Alpine–Dinaric System during the Paleogene–early Miocene (Kázmér & Kovács, 1985). This process probably involved

lithosphere-scale transport, as supported by the preservation of subduction-related geochemical features and deformation patterns in mantle xenoliths (Kovács & Szabó, 2008). The driving force for displacement (late Oligocene) and subsequent extension (Miocene) is considered to be subduction roll-back of the European plate beneath the ALCAPA unit along the Carpathian arc (Csontos & Vörös, 2004, and references therein) and collision-induced, eastward-directed mantle flow between the Apulian indenter and the stable European platform (Kovács & Szabó, 2008, and references therein). Extensive calc-alkaline volcanic activity occurred along the Carpathian Arc during the Neogene (Fig. 1). The developing Pannonian Basin was subsequently affected

Table 1: Modal abundance (v/v %) and major element composition (wt %) of mineral phases and silicate glasses in quartz-bearing orthopyroxene-rich websterite, Szigliget (BBHVF)

Phase:	opx	cpx	qz	glass non-heated		glass heated		glass non-heated								Bulk rock	
Note:				pr in opx		pr in opx		sec in opx		pr in cpx		sec in cpx		istgl			
Mode:	70	24	5	1*													
	av.	av.	av.	av.	range	av.	range	av.	range	av.	range	av.	range	av.	range		
	of 6	of 5	of 3	of 11		of 4		of 8		of 3		of 3		of 5			
SiO ₂	55.9	53.4	101.5	70.8	69.3–72.2	70.9	69.1–72.4	64.9	57.3–74.0	69.7	68.5–71.6	67.7	66.2–68.8	75.5	63.8–80.5	58.2	
TiO ₂	0.10	0.35	0.03	0.32	0.27–0.35	0.32	0.26–0.39	0.74	0.24–1.1	0.46	0.38–0.52	0.80	0.69–0.87	0.48	0.20–1.07	0.15	
Al ₂ O ₃	1.96	3.09	0.03	14.0	13.2–14.4	14.2	14.1–14.5	17.9	14.0–20.9	16.7	16.2–17.2	16.7	16.4–17.1	10.6	7.7–18.0	2.3	
Cr ₂ O ₃	0.29	0.70	0.12	0.01	0.00–0.02	0.01	0.00–0.01	0.01	0.00–0.02	n.d.		n.d.		0.02	0.02–0.03	0.35	
FeO	11.3	4.6	0.27	2.05	1.37–2.80	2.75	2.63–2.92	2.19	0.44–4.82	0.56	0.52–0.62	2.83	2.00–3.57	1.81	1.12–2.46	9.31	
MnO	0.11	0.08	0.04	0.03	0.00–0.06	0.04	0.04–0.05	0.06	0.00–0.12	n.d.		0.05	0.00–0.06	0.06	0.05–0.09	0.18	
NiO	0.25	0.11	n.a.	0.02	0.00–0.06	n.a.		0.03	0.01–0.05	n.a.		n.a.		n.d.	—		
MgO	30.0	15.5	0.02	0.40	0.10–1.01	0.88	0.76–1.11	0.10	0.00–0.24	0.02	0.00–0.03	0.33	0.08–0.63	0.35	0.05–0.91	24.3	
CaO	0.67	21.76	n.d.	1.34	0.97–1.67	1.36	1.02–1.56	2.62	1.16–3.50	2.19	1.93–2.56	1.62	1.15–1.90	1.39	0.69–3.06	5.57	
Na ₂ O	0.03	0.79	0.01	3.16	2.57–3.64	2.43	2.19–2.74	4.00	2.69–6.08	3.70	3.57–3.84	4.74	4.52–4.90	1.46	0.69–3.58	0.26	
K ₂ O	0.01	0.01	n.d.	4.82	3.70–5.27	5.11	4.80–5.87	4.21	2.72–5.59	4.13	3.98–4.33	3.89	3.47–4.58	4.83	4.45–5.18	0.05	
F	n.a.	n.a.	0.15	0.08	0.00–0.25	0.08	0.06–0.10	0.14	0.06–0.33	0.20	0.11–0.31	0.06	0.00–0.10	0.14	0.00–0.33	—	
SO ₃	n.a.	n.a.	n.a.	0.08	0.00–0.15	0.12	0.09–0.16	0.02	0.00–0.03	n.d.		0.03	0.00–0.03	0.02	0.00–0.03	—	
P ₂ O ₅	n.a.	n.a.	0.04	0.05	0.05–0.10	0.00	—	0.11	0.00–0.25	0.11	0.07–0.13	0.06	0.05–0.07	0.03	0.00–0.05	—	
Cl	n.a.	n.a.	n.a.	0.13	0.00–0.18	0.01	n.a.	0.18	0.08–0.34	0.16	0.15–0.16	0.12	0.11–0.15	0.09	0.02–0.24	—	
Total	100.7	100.3	102.2	97.2		98.3		97.2		97.9		98.9		96.7		100.7	
mg-no.	82.5	85.8	—	25.7		36.4		7.4		5.0		17.1		25.8		82.3	
cr-no.	—	13.2	—													9.29	
Na ₂ O/K ₂ O	—	—	—	0.66		0.48		0.95		0.90		1.22		0.30		5.35	

*Amount of primary melt inclusions.

Bulk-rock composition was estimated by mass-balance calculation. opx, orthopyroxene; cpx, clinopyroxene; qz, quartz; pr, primary melt inclusion; sec, secondary melt inclusion; istgl, interstitial glass vein; av. of 5, average of five analyses; n.d., not detected; n.a., not analysed.

by a short-lived ENE–WSW to east–west compressional event (Miocene–Pleistocene) (Fodor *et al.*, 1999) followed by extension. Alkaline basaltic volcanic activity occurred during the post-extension phase of basin formation (Embey-Isztin *et al.*, 1993), and included phreatomagmatic activity (Martin & Németh, 2004) at Szigliget at 3.4 Ma (Balogh *et al.*, 1986). The alkaline basalts contain abundant lower crustal and upper mantle xenoliths (Embey-Isztin *et al.*, 2001, 2003; Dobosi *et al.*, 2003a, 2003b; Török *et al.*, 2003; Szabó *et al.*, 2004), providing information on the composition and evolution of the regional lithosphere.

PETROGRAPHY

The Szg-klm01 xenolith is rounded, 3 cm in diameter, and free of secondary alteration. It is composed mainly of

large, tabular opx (up to 5.0 mm) and subordinate interstitial cpx (Table 1, Fig. 2a). It lacks both olivine and spinel. Opx and cpx contain large (up to 1 mm) rounded and/or euhedral, needle-shaped, transparent quartz (qz) single crystal inclusions (Fig. 2a–d). Needle-shaped qz inclusions usually occur as parallel laths in opx (Fig. 2b and c). Small (1–2 µm) CO₂ fluid inclusions occasionally occur near the tip of the needle-shaped qz inclusions, whereas silicate glass is associated only very rarely with them (Fig. 2c). This xenolith differs in texture and modal composition from the peridotite and pyroxenite xenoliths described from the same locality by other workers (e.g. Embey-Isztin *et al.*, 2001; Dobosi *et al.*, 2003a; Török *et al.*, 2003; Szabó *et al.*, 2004).

Silicate MI occur in both cpx and opx. All MI contain brownish to colourless silicate glass and a one-phase

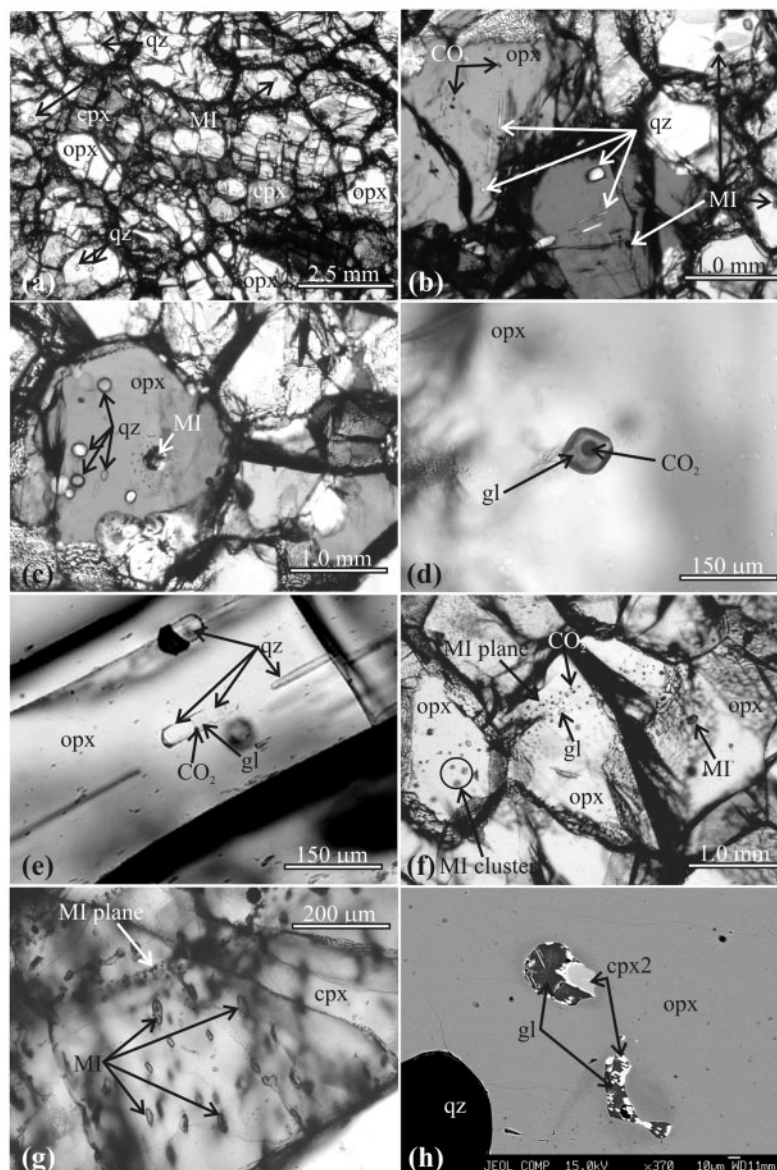


Fig. 2. Photomicrographs of textures and fluid and melt inclusions in the Szg-klm01 xenolith from Szigliget (BBHVF, West Hungary). (a) Orthopyroxenes (opx) and interstitial clinopyroxene (cpx) containing quartz (qz) and silicate melt inclusions (MI). Plane-polarized light. (b) Clusters of CO₂ fluid inclusions, parallel quartz (qz) laths and primary silicate melt inclusions (MI) in orthopyroxene (opx). Crossed polars. (c) Primary silicate melt inclusion (MI) associated with quartz (qz) in orthopyroxene (opx). Crossed polars. (d) Negative crystal-shaped, primary silicate melt inclusion in orthopyroxene. The melt inclusion consists of silicate glass (gl) and a CO₂ fluid phase. Plane-polarized light. (e) Elongated quartz (qz) laths trapped with silicate glass (gl) and a CO₂ fluid phase in orthopyroxene (opx). Plane-polarized light. (f) Primary silicate melt inclusion (MI) and a plane of secondary silicate melt inclusions (MI plane) cross-cutting orthopyroxene (opx) grain boundaries. The silicate melt inclusion plane contains both silicate glass-rich (gl) and CO₂ fluid-rich melt inclusions. Plane-polarized light. (g) Primary silicate melt inclusion (MI) assemblage and a secondary silicate melt inclusion plane (MI plane) cross-cutting clinopyroxene (cpx). Plane-polarized light. (h) Secondary silicate melt inclusions in orthopyroxene. The MI contain clinopyroxene (cpx2) daughter minerals, silicate glass and a fluid bubble. Also shown is a quartz (qz) inclusion. Backscattered electron image.

CO₂-fluid bubble at room temperature (Fig. 2c–f). Primary MI are large (50–150 µm in diameter), rounded or negative crystal shaped (Fig. 2d–g), and occur either as isolated inclusions (Fig. 2d–f) or in clusters (Fig. 2f and g) mainly in the cores of host opx and cpx. The glass:fluid volume

ratio is *c.* 10:1 to 15:1, and the MI never contain daughter minerals. Two generations of secondary MI (Fig. 2f–h) were distinguished. Both generations occur along healed fractures in opx and cpx (Fig. 2f–h). Secondary MI-1 are smaller (<30 µm in diameter) than the primary MI,

they have negative crystal or droplet shapes, and are composed of silicate glass and a fluid phase with variable glass: fluid ratios (Fig. 2f). They form inclusion planes cross-cutting grain boundaries (Fig. 2f). Secondary MI-2 have irregular shape (Fig. 2h). They occur along fractures close to grain boundaries where colourless silicate glass also occurs interstitially, forming $<10\ \mu\text{m}$ grain boundary films. In addition to the fluid bubble and silicate glass secondary MI-2 contain daughter minerals (Fig. 2h), which have approximately the same ratio in all secondary MI-2.

CO₂ fluid inclusions range from 5 to 25 μm and occur in both pyroxenes as isolated inclusions or in clusters (Fig. 2b).

ANALYTICAL TECHNIQUES

Raman spectroscopic analyses were conducted at ETH Zürich to identify the quartz inclusions and to determine the composition and density of the fluid inclusions and the water content of the glass. A Dilor Labram II system equipped with a 488 nm Ar⁺ laser source and confocal optics was used. Analysis and spectral treatment were carried out following the suggestions of Kawakami *et al.* (2003) for CO₂ and Zajacz *et al.* (2005) for H₂O measurements.

Primary MI in opx were heated in a N₂ atmosphere using a Linkam TS1500 heating-cooling stage at the Lithosphere Fluid Research Lab of Eötvös University, Budapest. A stepwise heating schedule was used (Student & Bodnar, 1999, 2004) and the experiment was quenched by turning the power off.

Major element analysis of host minerals (Table 1) was carried out using the JEOL Superprobe JXA-8600 WDS at the Electron Microprobe Laboratory of the CNR–Institute of Geosciences and Earth Resources of Florence, Italy [conditions have been described by Vaselli *et al.* (1996)]. MI were analysed using a CAMECA SX50 microprobe at the Department of Geosciences, Virginia Tech [conditions have been described by Szabó *et al.* (1996)] and a Jeol Superprobe JXA-8200 at the Bayerisches Geoinstitut (BGI), Germany. Analyses at the BGI were carried out with an accelerating voltage of 15 kV, beam current of 20 nA and beam size of 5 μm . Counting time for each element was 10 s. Natural and synthetic standards were used for calibration and ZAF correction was applied.

Laser ablation inductively coupled plasma mass spectrometry (LA-ICPMS) analyses were carried out at ETH Zürich, using an ArF excimer UV (193 nm) laser source at 70 mJ output energy and 10 Hz repetition rate. The beam diameter was 20–80 μm and 10 ms dwell time was used for all elements. The energy density was homogeneous across the laser beam profile (Heinrich *et al.*, 2003). Quantification of MI compositions followed the method of Halter *et al.* (2002) and K₂O from electron microprobe

analysis was used as an internal standard. Sample NBS SRM 610 was used for external standardization. Results are given in Table 2.

RESULTS

Raman spectroscopy and heating experiments

Raman analyses confirm that all solid inclusions in the opx and cpx are quartz crystals with two significant vibration bands at 461.9 and 205.3 cm^{-1} . The Raman spectra show no evidence of conversion from an earlier high-temperature polymorph (i.e. cristobalite–tridymite, e.g. Darling *et al.*, 1997; Hirose *et al.*, 2005), which has vibration bands at different wavenumbers. The fluid phase is pure CO₂ regardless of whether it occurs in fluid inclusions or in melt inclusions. Eight CO₂ fluid inclusions in opx were analysed by Raman spectroscopy. CO₂ density in these inclusions was calculated using the method of Kawakami *et al.* (2003), who found that the distance between the two main CO₂ vibration bands of the Fermi diad at 1388 cm^{-1} and 1285 cm^{-1} is related to the density of the fluid. This distance varies between 105.5 and 104.4 cm^{-1} , corresponding to a range in density from 1.17 to 0.82 (± 0.03) g/cm^3 . The highest density CO₂ fluid inclusion in this xenolith ($\rho = 1.17\ \text{g/cm}^3$) is higher than that of any of the primary fluid inclusions in lower crustal granulite or peridotite xenoliths previously analysed from the BBHVF (Török & De Vivo, 1995; Török *et al.*, 2005; Berkesi *et al.*, 2007). The H₂O content of the glass in the MI was below the detection limit of $\sim 1\ \text{wt}\ \%$. During heating on the Linkam stage, the MI decrepitated before complete dissolution of the CO₂ fluid phase into the melt. Thus, only the onset (840–880°C; average 860°C) and termination (915–980°C; average 960°C) of glass melting were observed and recorded (Fig. 3a).

Major and trace element chemistry

Opx in the websterite is Fe-rich (average mg-number = 81.7) and Al₂O₃-poor (*c.* 2 wt %), compared with opx in olivine websterite, lherzolite and pyroxenite xenoliths from the same area (Embey-Isztin *et al.*, 2001; Török *et al.*, 2003; Dobosi *et al.*, 2003b; Bali *et al.*, 2007). However, the opx grains in the studied xenolith have higher mg-number and significantly lower CaO compared with those in the local granulite xenoliths (Embey-Isztin *et al.*, 2003) (Fig. 4). Cpx has higher mg-number (average 86.0) than coexisting opx (Table 1, Fig. 4), and a slightly lower mg-number than that of cpx in olivine websterite, peridotite and pyroxenite xenoliths from the BBHVF; however, it is higher than the mg-number of cpx in local granulite xenoliths (Fig. 4). The Si/Al ratio of cpx is similar to that of cpx in BBHVF peridotite and opx-rich ol-websterites, and significantly higher than in clinopyroxenite and granulite xenoliths (Fig. 4). The Cr₂O₃ content in

Table 2: Trace element composition (ppm) of mineral phases and silicate glasses in quartz-bearing orthopyroxene-rich websterite, Szegliget (BBHVF)

	silmi pr in opx		silmi sec in opx		silmi pr in cpx		Cpx		Opx	
	av. of 7	SD of 7	av. of 2	SD of 2	av. of 3	SD of 3	av. of 7	SD of 7	av. of 14	SD of 14
P	286.47	57.90	257.51	22.82	240.46	32.87	38.86	10.65	28.78	5.46
Sc	1.46	0.96	1.92		9.02	7.52	29.84	4.28	6.15	0.86
V	15.37	10.42	9.18	2.93	16.01		138.26	26.13	49.23	23.61
Cr	272.46	137.32	252.87	93.50	738.80	112.45	4203.45	91.05	1770.78	156.59
Ni	389.77	209.18	389.68	61.53	765.26		855.41	83.75	1549.41	301.71
Cu	7.09	3.40	5.45	0.65	7.25	1.94	1.22	0.38	1.36	0.20
Rb	272.21	61.91	269.30	8.22	188.44	52.55	0.05	0.02	0.06	0.01
Sr	89.84	13.95	88.78	0.56	81.57	7.57	19.44	1.16	0.04	0.01
Y	6.26	2.05	5.40	0.11	17.20	13.59	23.82	1.96	1.70	0.51
Zr	216.59	26.12	216.99	2.13	196.23	39.43	60.83	5.07	2.78	0.37
Nb	1.54	0.28	1.43	0.07	1.55	0.52	0.03	0.00	0.01	
Ba	709.34	125.17	662.73	53.62	700.81	105.95	0.24	0.12	0.18	0.12
Cs	9.62	15.30	16.56	18.23	1.49	0.90	<0.01		0.01	0.00
La	72.62	10.05	69.76	0.27	69.21	7.35	17.09	0.53	0.03	0.01
Ce	128.18	19.13	120.00	3.97	126.20	19.56	67.14	2.74	0.19	0.05
Nd	36.21	4.82	36.32	1.22	57.36	25.63	56.61	3.36	0.36	0.10
Sm	4.44	0.75	4.22	0.19	11.85	10.53	13.19	0.76	0.19	0.04
Eu	1.12	0.19	1.06	0.16	2.12	1.52	2.67	0.19	0.04	0.01
Gd	2.39	0.77	2.34	0.02	6.58	6.69	10.05	0.65	0.22	0.05
Yb	0.59	0.09	<0.36		2.06	1.21	1.38	0.19	0.26	0.11
Lu	0.07	0.03	0.06		0.13		0.16	0.03	0.04	0.02
Hf	5.49	0.84	4.90	0.12	6.03	0.59	2.41	0.11	0.10	0.03
Ta	0.12	0.04	0.14	0.01	0.14	0.03	0.02	0.01	<0.01	
Pb	20.35	5.23	18.77	0.17	15.80	3.50	0.47	0.08	0.04	0.00
Th	54.11	7.26	54.82	1.27	44.75	4.20	0.30	0.07	0.02	0.01
U	6.18	1.12	5.57	0.07	5.15	0.34	0.03	0.01	<0.01	
Pr	11.58	1.43	10.72	0.26	15.48	5.04	11.14	0.56	0.05	0.01
Er	0.54	0.09	0.55		1.83		2.05	0.24	0.22	0.12
Ho	0.25	0.07	0.20		1.17	1.26	0.94	0.13	0.07	0.02
Tb	0.34	0.06	0.33	0.00	0.47		1.26	0.14	0.04	0.01
Li	36.17	11.69	39.78	6.37	37.43	3.92	13.33	0.43	11.97	1.32
La _N /Sm _N	10.24		10.37		3.66		0.81		0.10	
Sm _N /Yb _N	8.36		12.94		6.34		10.56		0.81	
La _N /Yb _N	85.63		134.18		23.22		8.57		0.08	
Ba _N /Nb _N	48.49		48.72		47.58		0.83		3.67	
Nb _N /La _N	0.02		0.02		0.02		0.00		0.15	
Sr/Y	14.36		16.45		4.74		0.82		0.02	
La/Yb	123.7		193.8		33.5					
Ba/La	9.77		9.50		10.13					

av. of 5, average of five analyses. Normalized according to McDonough & Sun (1995). silmi, silicate melt inclusions; pr, primary; sec, secondary; Cpx, clinopyroxene; Opx, orthopyroxene.

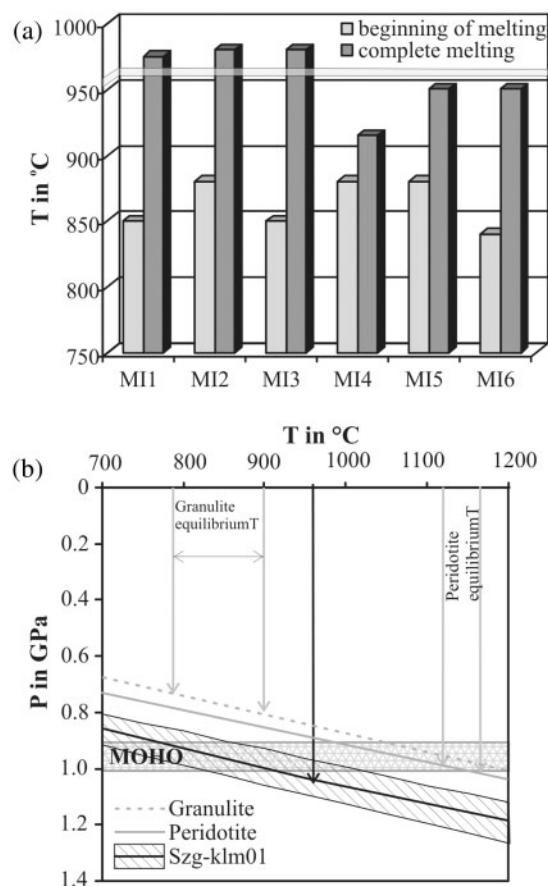


Fig. 3. Results of heating experiments on melt inclusions and pressure and temperature estimates for the Szg-klm01 xenolith. (a) Results of heating experiments on primary melt inclusions (MI) in orthopyroxene. Light grey columns show the temperature of beginning of glass melting; dark grey columns show the temperature of complete melting of silicate glass in MI. Light shaded horizontal band at $\sim 950^{\circ}\text{C}$ is the average glass melting temperature. (b) Comparison of fluid isochors of high-density CO_2 fluid inclusions from xenolith Szg-klm01, orthopyroxene-rich peridotites (Berkési *et al.*, 2007) and lower crustal granulites (Török *et al.*, 2005). Cross-hatched field shows the uncertainty of the calculated isochor (see text). Grey arrows indicate the equilibrium temperature ranges of lower crustal granulites and orthopyroxene-rich peridotites; the black arrow shows the melting temperature of MI in Szg-klm01. Moho depth is from Lenkey (1999).

cpx is higher than that in BBHVF clinopyroxenite and granulite xenoliths, but falls in the range characteristic for local peridotite and olivine websterite xenoliths (Fig. 4). The Na_2O content in cpx is lower than that in BBHVF clinopyroxenite xenoliths, falling in the range of peridotite, olivine websterite and granulite xenoliths from the region (Fig. 4).

All silicate glasses are depleted in MgO (≤ 10 wt %), FeO (≤ 3.6 wt %) and CaO (≤ 3.3 wt %), and rich in SiO_2 (58–81 wt %) and alkalis ($\text{Na}_2\text{O} + \text{K}_2\text{O}$ 4.0–9.5 wt %), with variable Al_2O_3 contents (7.0–20.9 wt %). This last variation is most pronounced in the interstitial silicate

glass (Fig. 5, Table 1). Silicate glass in primary MI in cpx and opx shows little chemical variation (Fig. 5, Table 1); however, slight differences occur in the FeO , MgO , CaO and Al_2O_3 contents. FeO (0.5–0.6 wt %) and MgO (≤ 0.02 wt %) contents are lower, whereas CaO (1.93–2.56 wt %) and Al_2O_3 (16.2–17.2 wt %) contents are higher in cpx-hosted primary MI compared with primary MI in opx (1.5–2.8, 0.2–1.05, 1.22–1.67 and 13.6–14.4 wt %, respectively). Glasses in all primary MI display consistent high $\text{K}_2\text{O}/\text{Na}_2\text{O}$ ratios (1.1–1.8). Reheated primary MI in opx have SiO_2 (66–72 wt %) and MgO (0.6–1.0 wt %) contents similar to those of the most SiO_2 -poor and MgO -rich, non-heated MI (Fig. 5a, Table 1). Compared with the primary MI, secondary MI and interstitial glass have a wide compositional range that includes the compositions of primary MI (Fig. 5). Secondary MI-1 in both cpx and opx contain silicate glass similar in composition to glass in primary MI (Fig. 5). SiO_2 -rich (*c.* 80 wt %) interstitial glass occurs between qz and opx, whereas glass along opx–cpx boundaries and in secondary MI-2 is significantly poorer in SiO_2 and enriched in other major elements (Fig. 5, Table 1).

Cpx is strongly enriched in light rare earth elements (LREE) and middle REE (MREE) compared with heavy REE (HREE) (Table 2), with significant negative anomalies for Pb, Sr, Hf, Zr and Ti on primitive mantle-normalized trace element diagrams (Fig. 6a). These clinopyroxenes are more enriched in LREE and MREE, but more depleted in Sr than those in local peridotite, pyroxenite and granulite xenoliths (Fig. 6a and b). Opx in the studied xenolith is depleted in LREE and MREE compared with HREE (Fig. 6a, Table 2). However, both cpx and opx in the xenolith show enrichment in incompatible elements compared with cpx and opx from BBHVF peridotites (Fig. 6b). Both cpx and opx have high concentrations of Cr (4200 and 1770 ppm, respectively) and Ni (855 and 1550 ppm, respectively), the latter being about two times higher than in pyroxenes in local peridotite xenoliths (Fig. 6b).

Primary MI in both pyroxenes were analysed for trace elements, whereas only secondary MI-1 in opx were analysed. MI compositions show a narrow range, independent of host mineral and textural features (Fig. 6c, Table 2). Primary MI and secondary MI-1 are strongly enriched in incompatible elements and display negative anomalies for Nb, Ta and Sr, and a slight positive anomaly for Pb (Fig. 6c, Table 2). The REE pattern is particularly steep ($\text{La}_\text{N}/\text{Yb}_\text{N}$ 85–134).

Crystallization conditions

The coexistence of CO_2 inclusions with MI suggests that the melt became saturated in CO_2 during crystallization. The pressure of formation of fluid inclusions may be determined if the density (or homogenization temperature) of the inclusions and the formation temperature are

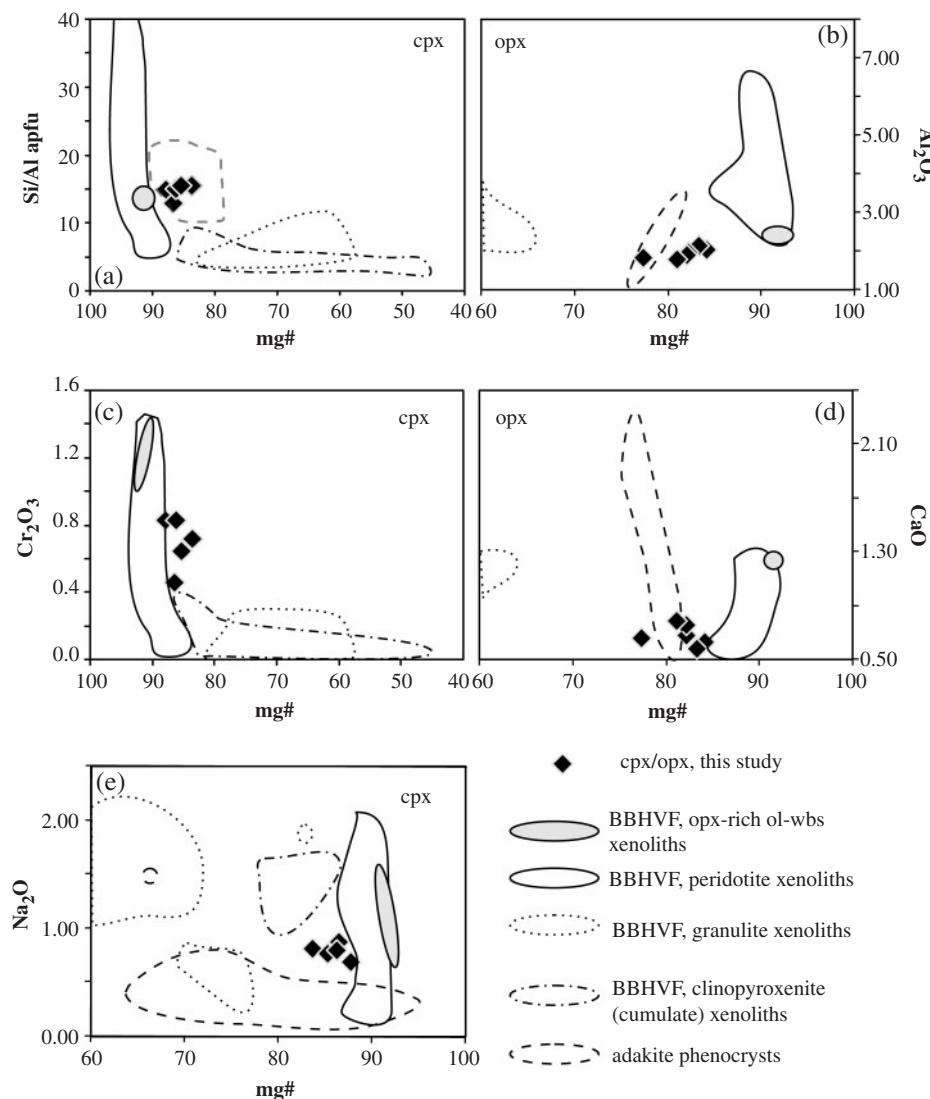


Fig. 4. Composition of clinopyroxenes (a, c, e) and orthopyroxenes (b, d) from the Szg-klm01 xenolith (Szigliget, BBHVF, West Hungary). For comparison compositional fields of clino- and orthopyroxenes from BBHVF peridotite (Embey-Isztin *et al.*, 2001), cumulate (Dobosi *et al.*, 2003a; Török *et al.*, 2003) and mafic granulite xenoliths (Embey-Isztin *et al.*, 2003), as well as adakite phenocrysts (Sajona *et al.*, 2000) are also shown.

known (Bodnar, 2003a), assuming that the density does not change after trapping. However, the density may decrease during transport to the surface as a result of stretching of the host mineral (e.g. Bodnar, 2003b) or leakage along crystal dislocations (e.g. Viti & Frezzotti, 2000; Vityk *et al.*, 2000), and evidence for such re-equilibration is usually not recognizable during routine petrographic observation. As a result of re-equilibration the density of the inclusions is less than the original density of the fluid inclusion at trapping. The highest density inclusion most closely approximates the true density, but still represents the minimum entrapment conditions. Thus, in xenolith Szg-klm01, the highest density CO_2 inclusion gives the closest, but still a minimum, estimate for the pressure of formation of

the rock. The formation pressure of Szg-klm01 estimated using the equation of state of Mader & Berman (1991) and assuming an entrapment temperature of 960°C (based on MI thermometry) was above 1.1 GPa (Fig. 3b).

Considering that the present-day depth to the Moho in this area is $\sim 27\text{--}30$ km, which corresponds to $\sim 0.9\text{--}1.0$ GPa (Lenkey, 1999), the CO_2 inclusions in this rock must have been trapped in the uppermost mantle, where the rock presumably also formed.

DISCUSSION

The Szg-klm01 xenolith differs in mode, texture and phase composition from peridotite and pyroxenite xenoliths from

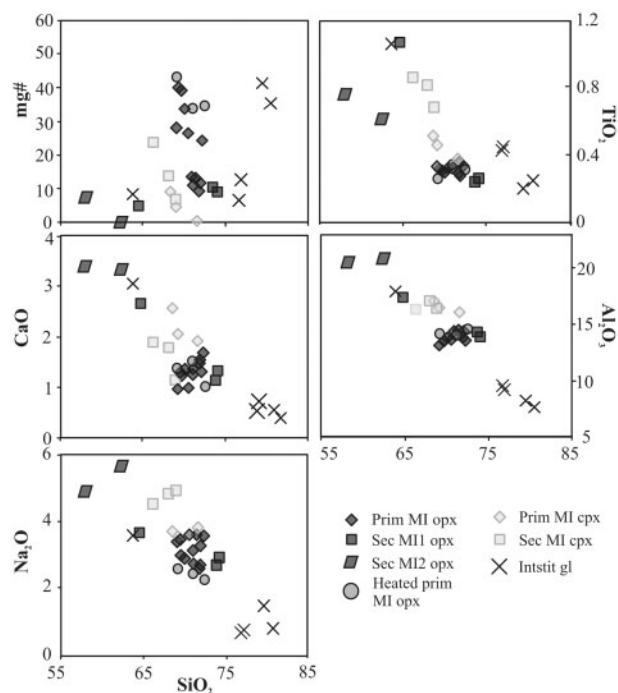


Fig. 5. Composition of silicate glass in silicate melt inclusions (MI) and interstitial veins from the Szg-klm01 xenolith (Szigliget, BBHVF, Western Hungary). prim MI, primary silicate melt inclusion; sec MI, secondary silicate melt inclusion; sec MI2, second generation of secondary silicate melt inclusions; interstit gl, interstitial glass; opx, orthopyroxene; cpx, clinopyroxene.

the same volcanic field (Embey-Isztin *et al.*, 2001; Dobosi *et al.*, 2003b; Török *et al.*, 2003; Bali *et al.*, 2007). Szg-klm01 has an igneous texture, but does not contain olivine and spinel as do the clinopyroxenite and opx-rich websterite cumulate xenoliths from the same locality (Dobosi *et al.*, 2003b; Bali *et al.*, 2007); however, importantly, it does contain qz. The needle-shaped qz inclusions in most cases seem to follow the crystallographic directions of opx, but an exsolution origin can be ruled out as the opx does not show 'super-siliceous' composition compared with the BBHVF mantle opx (SiO_2 53.08–56.51 wt %; see Downes *et al.*, 1992; Embey-Isztin *et al.*, 2001) and the qz crystals are frequently associated with CO_2 and occasionally silicate glass (Fig. 2b and c), which could not exsolve from opx. Moreover, qz cannot be interpreted as a daughter mineral of the primary MI because this would require a near-constant ratio of fluid:silicate glass:qz in all inclusions from the same MI generation, which is not observed (Fig. 2). Thus, we suggest that qz nucleated on the growing opx and was entrapped with the CO_2 fluid and occasionally with melt as the opx continued to grow.

The cpx shows a much stronger enrichment in LREE and especially MREE ($\text{La}_N/\text{Yb}_N = 8.6$, $\text{Sm}_N/\text{Yb}_N = 10.6$) and depletion in Sr compared with cpx from local cpx- and opx-rich cumulates ($\text{La}_N/\text{Yb}_N = 1.6$ – 2.1 and 0.9 – 2.5 , $\text{Sm}_N/\text{Yb}_N = 2.6$ – 4.2 and 0.2 – 0.7 , respectively),

residual peridotites ($\text{La}_N/\text{Yb}_N = 0.4$ – 1.1 , $\text{Sm}_N/\text{Yb}_N = 0.9$ – 1.0) or granulites ($\text{La}_N/\text{Yb}_N = 1.2$ – 5.9 , $\text{Sm}_N/\text{Yb}_N = 8.2$ – 23.3) (Fig. 6a and b).

Significant modal and chemical differences are observed between the studied xenolith and opx-rich harzburgites and orthopyroxenites from ultramafic xenolith suites from supra-subduction zone tectonic settings worldwide (e.g. Parkinson & Pearce, 1998; McInnes *et al.*, 2001; Melcher *et al.*, 2002; Santos *et al.*, 2002; Cvetkovic *et al.*, 2004). Ultramafic xenoliths from supra-subduction zone tectonic settings usually contain refractory opx (mg-number usually >90), Cr-rich spinels and cpx displaying U-shaped chondrite-normalized REE patterns. In contrast, opx in Szg-klm01 is relatively Fe-rich (mg-number = 82) and cpx is strongly enriched in both LREE and MREE compared with HREE.

Interaction of mantle lherzolite with a SiO_2 -rich melt

SiO_2 -rich melts responsible for some mantle metasomatism can be produced by extensive reaction between peridotite and basaltic melt (Wulff-Pedersen *et al.*, 1996, 1999; Neumann & Wulff-Pedersen, 1997). The basaltic melt mainly dissolves the trace element-poor orthopyroxenes of the peridotites. Dissolution of significant amounts of wall-rock opx might lead to elevated SiO_2 contents in the melt, but the melt will not be silica-oversaturated and will not crystallize quartz in the upper mantle. Furthermore, dissolution of opx leads to dilution of incompatible trace element contents in the melt. Wulff-Pedersen *et al.* (1999) have shown that migrating silicate melts with the highest SiO_2 contents have concave (MREE-depleted) trace element patterns with marked positive anomalies of Ba and Sr. As interaction between peridotite and basaltic melt (1) does not produce qz, (2) dissolves but does not precipitate opx, and (3) produces trace element patterns of the melt that differ strongly from those observed in the MI of the studied xenolith (Fig. 6c–f), this process cannot be the source of the SiO_2 -rich melt.

In contrast, Arai *et al.* (2003), Bianchini *et al.* (2004) and Shimizu *et al.* (2004) have described slab-derived qz-diorite veins cross-cutting peridotite xenoliths from Tallante, Spain. In these xenoliths, opx-rich bands developed at the boundary between peridotite and the qz-diorite vein, representing the reaction product of silicic melt and wall-rock (Arai *et al.*, 2003; Shimizu *et al.*, 2004). During this reaction, olivine and clinopyroxene in the wall-rock peridotite are dissolved. Olivine dissolution leads to orthopyroxene saturation in the SiO_2 -rich melt at the peridotite–melt interface, causing crystallization of orthopyroxene (e.g. Morgan & Liang, 2005).

The above interpretation is consistent with phase relations in the fo–di–qz ternary at 2 GPa (Kushiro, 1969). Experimental slab melts fall in the qz-in liquidus field (Fig. 7), so qz will crystallize first from silicic slab melts

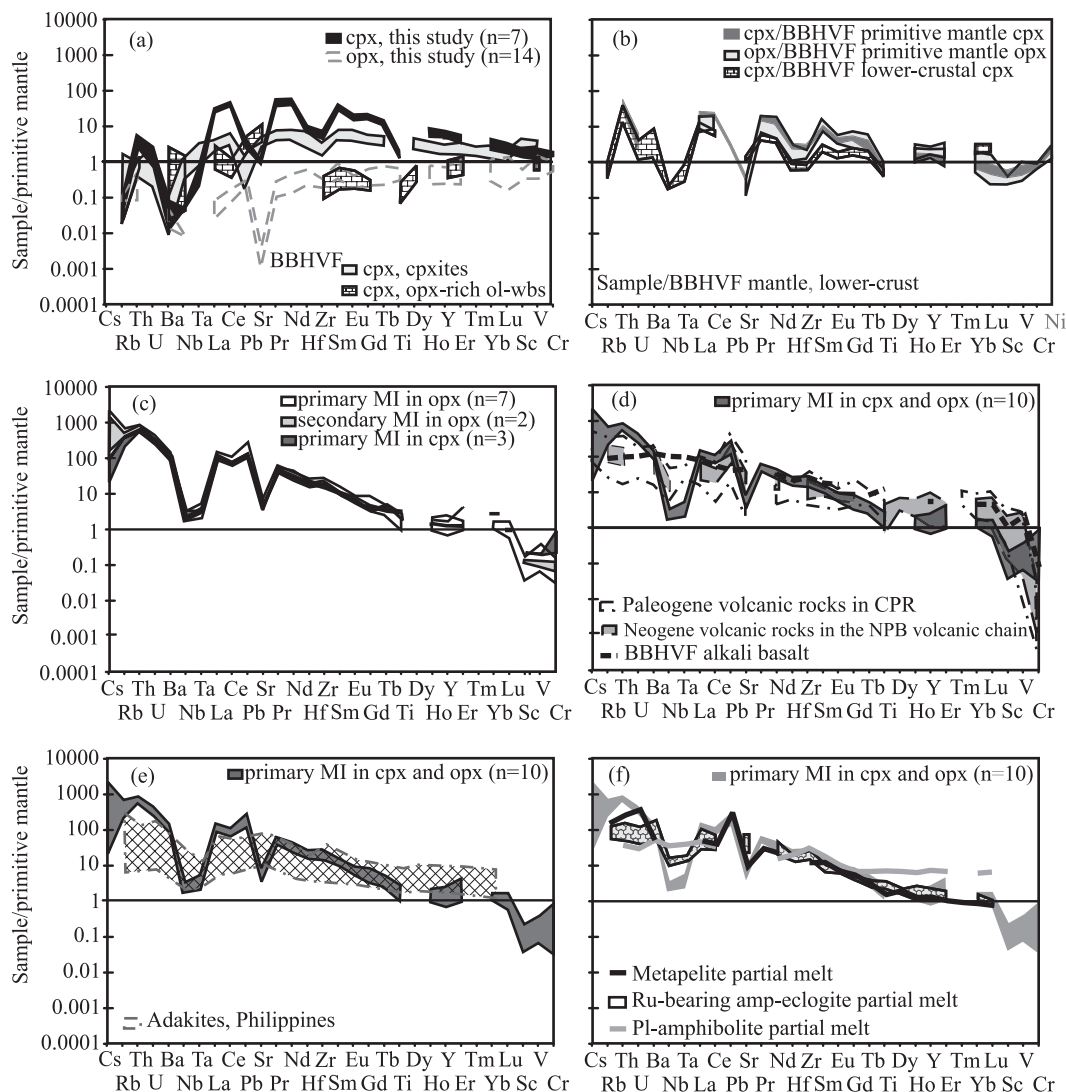


Fig. 6. Primitive mantle normalized trace element diagram for ortho- and clinopyroxenes (opx and cpx) (a), and silicate melt inclusions (MI) (c–f) from the Szg-klm01 xenolith (Szigliget, BBHVF, Western Hungary). For comparison the composition of cpx from cpx- and opx-rich cumulate xenoliths (Dobosi *et al.*, 2003a; Bali *et al.*, 2007) (a), Paleogene and Neogene calc-alkaline andesites from Pannonian Basin (Harangi *et al.*, 2001; Benedek *et al.*, 2004) and BBHVF alkali basalts (Embey-Isztin *et al.*, 1993) (d), natural adakites (Prouteau *et al.*, 2000; Sajona *et al.*, 2000) (e), and partial melts of metabasalts and metapelites (i.e. Garcia-Casco *et al.*, 2001; Xiong, 2006) (f), are also shown. Data are normalized to the primitive mantle composition of McDonough & Sun (1995). In (b) the compositions of cpx and opx from the Szg-klm01 xenolith are normalized to 'BBHVF primitive mantle cpx and opx' determined by Dobosi (2003) and the average cpx composition in BBHVF granulites (Dobosi, 2003). opx, orthopyroxene; cpx, clinopyroxene; MI, silicate melt inclusion; amp, amphibole; pl, plagioclase; ru, rutile; CPR, Carpathian–Pannonian Region; NPB, Northern Pannonian Basin.

at mantle depths. In contrast, silicate melts formed by partial melting of peridotite are usually nepheline and olivine normative and fall in the ol-in liquidus field (Fig. 7). Thus, based on experimental data, the Mg/Si ratio in a continuously evolving slab–trondjemitic melt will increase during hybridization and its composition will move first into the opx + liquid field and later to the opx + cpx cotectic line. A similar evolution is observed in natural adakites (Fig. 7). In the initial stage of hybridization, when the ratio of peridotite to SiO₂-rich melt is low, a hybrid melt that is

still silica-oversaturated could form and crystallize qz and opx as observed in the studied xenolith. This scenario requires a high melt/wallrock ratio, which would be maintained if the SiO₂-rich melt migrated along fractures.

Model calculations were carried out to estimate the ratio of slab melt and assimilated wallrock peridotite in the bulk composition of the studied xenolith (Fig. 7). The peridotite component was approximated using the modal and major element composition of a protogranular peridotite xenolith from the same location (Szt1017, reported by

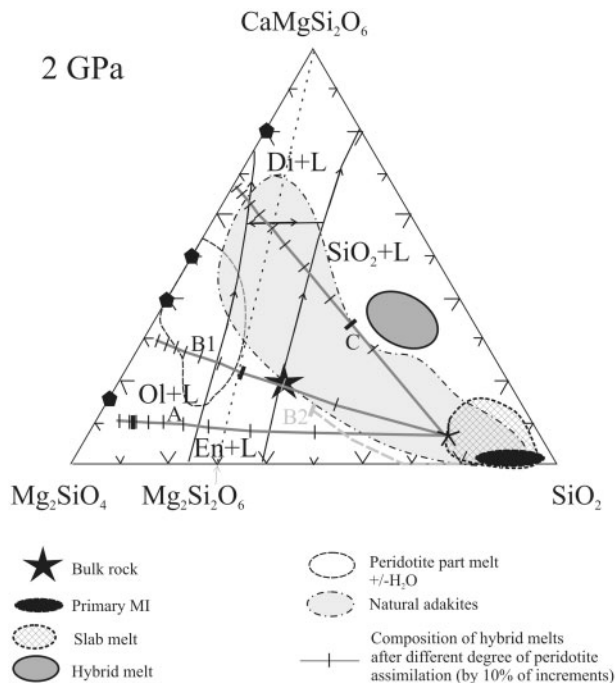


Fig. 7. Liquidus phase relations in the forsterite (ol)– SiO_2 –diopside (di) ternary diagram at 2 GPa (Kushiro, 1969). Arrows show the direction of decreasing T along univariant lines. Compositions of hybrid melts developed by dissolution of peridotite in slab melt are shown by Paths A, B1, B2 and C. Starting materials for the calculations were Szt1017 protogranular lherzolite (Downes *et al.*, 1992) and a slab melt released at 1.6 GPa and 1000°C from a metabasalt with N-MORB composition (Rapp & Watson, 1995) and at 1.3 GPa and 950°C from a metasediment (Patiño-Douce & Beard, 1995) (Path B2). During the calculation the ratio of dissolved cpx and ol was varied. Path A shows the hybrid melt composition after peridotite dissolution in a ratio corresponding to the modal cpx and opx content of xenolith Szt1017. Paths B1, B2 and C correspond to peridotite dissolution in which the cpx:ol is 40:60, 50:50 and 80:20, respectively. Tick marks along the path lines are 10% increments; thick tick marks indicate the complete dissolution of cpx from the starting peridotite xenolith. For comparison, partial melts of spinel peridotite (Falloon *et al.*, 1997; Gaetani & Grove, 1998), metabasalts (Rapp *et al.*, 1999; Hermann & Green, 2001; Skjerlie & Patiño-Douce, 2002), hybrid melt after slab melt–peridotite interaction (Rapp *et al.*, 1999) and natural adakites (Prouteau *et al.*, 2000; Sajona *et al.*, 2000) are also shown.

Downes *et al.*, 1992), whereas the experimental ‘slab melt’ composition (formed from metabasalts) of Rapp & Watson (1995) was used for the silicic melt. Path A in Fig. 7 shows the variation in the normative composition of the hybrid melt when the modal ol and cpx abundances of Szt1017 dissolve. The reaction product is depleted in normative cpx compared with the studied xenolith. This suggests that the SiO_2 -rich melt probably dissolved cpx and ol selectively from the peridotitic wallrock, rather than in their modal proportions. Our calculations indicate that the normative composition of Szt1017 xenolith can be generated by dissolution of ~20 wt % of peridotite wallrock, in which the ratio of dissolved ol:cpx was 3:2

(Path B in Fig. 7). These parameters yield a cpx-free harzburgite wallrock after 30 wt % of assimilation. In the case of a significantly higher (4:1) cpx:ol dissolution ratio (Path C in Fig. 7), the reaction product will be cpx-rich. On the other hand, for such a high cpx:ol dissolution ratio, the calculations require a cpx-rich peridotite or pyroxenite for the assimilated wallrock, because the modal composition of the Szt1017 xenolith allows a maximum of 15 wt % of assimilation before cpx is completely dissolved. The high Ni and Cr concentrations in the pyroxenes and in the primary and secondary MI (Table 2) are also explained by dissolution of peridotite because mantle lherzolite contains high concentrations of these refractory elements.

Based on model calculations and petrographic evidence, the opx-rich composition of the studied xenolith can be explained by crystallization of $\text{qz} + \text{opx} \rightarrow \text{qz} + \text{cpx}$ from a hybrid melt that developed at the interface between peridotite and SiO_2 -rich melt after a small degree of peridotite assimilation. The hybrid melt predicted by the model calculation is SiO_2 - and Na_2O -rich (~60 and ~6 wt %, respectively), with moderate Al_2O_3 and low CaO contents (~15 and ~4 wt %, respectively) and high mg-number (~75) (Fig. 8). It falls between the fields of peridotite partial melts (e.g. Falloon *et al.*, 1997; Gaetani & Grove, 1998) and slab melts formed from metabasalts or metasediments (e.g. Rapp & Watson, 1995; Rapp *et al.*, 1999; Hermann & Green, 2001; Skjerlie & Patiño-Douce, 2002) and is close to compositions of experimental hybrid melts (Rapp *et al.*, 1999) and natural adakites (Prouteau *et al.*, 2000; Sajona *et al.*, 2000); however, the mg-numbers of the experimental hybrid melts and natural adakites are lower (Fig. 8).

Origin and significance of MI

Both heated and unheated primary MI trapped in opx have a restricted range in concentration of all major elements with the exception of MgO, FeO, mg-number and SiO_2 (Table 1, Fig. 5). This variability is consistent with the varying degree of host mineral crystallization on inclusion walls after entrapment of the MI and, in the case of the heated inclusions, possibly the remelting of host mineral during the heating experiments. It is well known that, following the entrapment of MI, crystallization of the host mineral on the inclusion wall might be significant (e.g. Frezzotti, 2001; Bodnar & Student, 2006). Because of the lack of any compositional gradient around the MI, the amount of crystallization cannot be estimated properly. However, the mg-number of melts in equilibrium with the host opx and cpx can be calculated using the relevant Fe–Mg exchange coefficient [$K_d^{\text{Fe-Mg}} = (\text{FeO}_{\text{mineral}} \times \text{MgO}_{\text{melt}}) / (\text{FeO}_{\text{melt}} \times \text{MgO}_{\text{mineral}})$]. Applying K_d values of 0.27 for opx (Kinzler & Grove, 1992) and 0.275 for cpx (Putirka *et al.*, 2003), mg-numbers of equilibrium melts are 54–56 and 61–63 for opx and cpx,

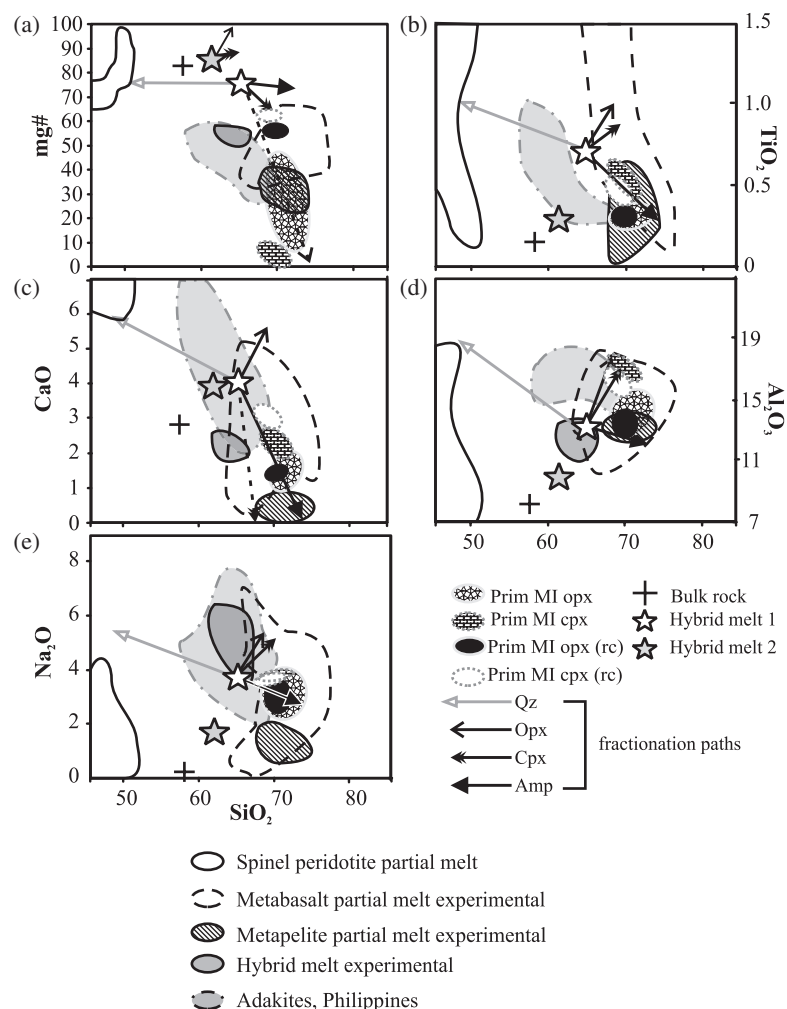


Fig. 8. Calculated effect of fractional crystallization on the major element composition of a hybrid melt. For comparison, partial melts of spinel peridotite (Falloon *et al.*, 1997; Gaetani & Grove, 1998), metabasalt (Rapp & Watson, 1995; Rapp *et al.*, 1999; Hermann & Green, 2001; Skjerlie & Patiño-Douce, 2002), metapelite (Patiño-Douce & Johnston, 1991), experimental hybrid melt (Rapp *et al.*, 1999) and adakites (Proureau *et al.*, 2000; Sajona *et al.*, 2000) are also shown. Stars indicate the proposed hybrid melt composition; arrows show qz, opx, cpx and amp (Szb55 amp of Bali *et al.*, 2002) fractionation trends (30 wt% each, except for the dashed arrows, which are <30 wt% for opx in (a) and <20 wt% for cpx in (c)). prim MI, primary silicate melt inclusion; rc, corrected with post-entrapment crystallization; Hybrid melt 1, 2, calculated hybrid melt compositions (see the text); qz, quartz; opx, orthopyroxene; cpx, clinopyroxene; amp, amphibole.

respectively, corresponding to about 3.0–5.5 wt % of post-entrapment crystallization of opx and cpx on MI walls. It should be noted that re-equilibration of the MI with the host mineral could have occurred, which would change the Fe/Mg ratio of the trapped melt (see, e.g. Danyushevsky *et al.*, 2000), so the above value is only an approximation of the extent of post-entrapment crystallization. However, such a small degree of post-entrapment crystallization would not change significantly the original composition of the MI, with the exception of the MgO and FeO contents and mg-numbers (Fig. 8). This suggests that the melt trapped in equilibrium with opx has a higher SiO_2 content, and lower TiO_2 , CaO and Na_2O contents and mg-number than calculated for a hybrid melt having

a metabasaltic source (Fig. 8). The low TiO_2 and Na_2O can be explained if the reagent melt was released from metasediments, but the low CaO cannot be explained by the simultaneous crystallization of opx + qz from a hybrid melt developed from either metabasaltic or metasedimentary slab melts (Fig. 8). The low CaO contents require the precipitation of a CaO-rich phase, different from the cpx crystallized after entrapment of the opx-hosted MI. Such a CaO-rich phase does not occur in the assemblage, but one might have developed in the reagent SiO_2 -rich melt or in the peridotite wallrock. This phase could be amphibole (amp), which is widespread in the regional upper mantle (e.g. Embey-Isztin, 1976; Embey-Isztin *et al.*, 1989; Downes *et al.*, 1992; Bali *et al.*, 2008).

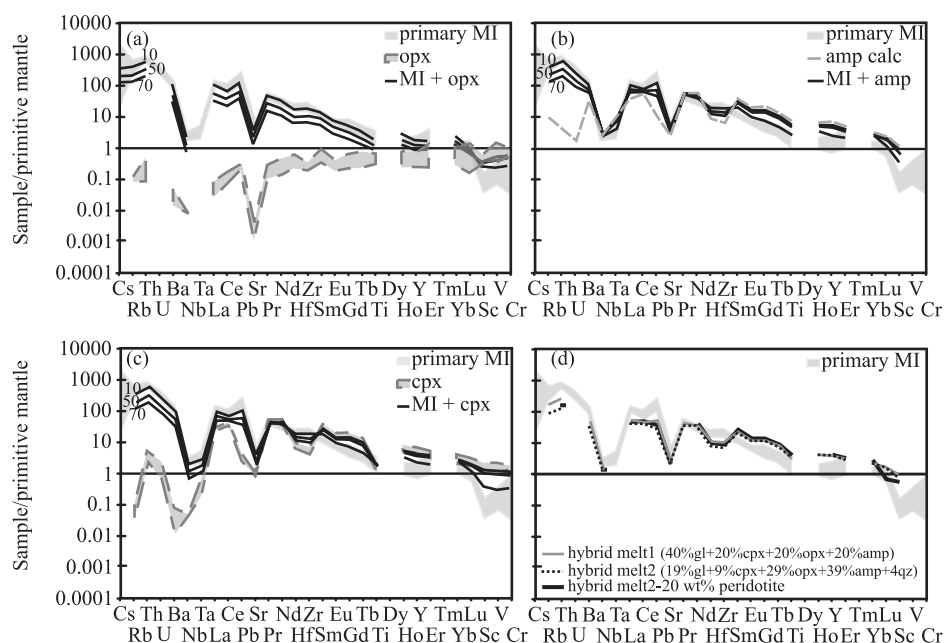


Fig. 9. Calculated effect of fractional crystallization on the trace element composition of a hybrid melt. Orthopyroxene (a), amphibole (b) and clinopyroxene (c) were added in different ratios to the average silicate melt inclusion composition to reproduce the possible hybrid melt composition after various (10, 50, 70%) degrees of fractional crystallization of each mineral. (d) indicates the combined effect of orthopyroxene + clinopyroxene + amphibole (+ quartz) addition and the continuous line is an estimate of the slab-melt composition after the extraction of 20 wt % of peridotite with a clinopyroxene:olivine ratio of 40:60 (see the text and Fig. 6). For this last calculation the trace element composition of clinopyroxene and olivine in the Szgl080 protogranular xenolith (Dobosi *et al.*, 2003b) was used. MI, silicate melt inclusion; qz, quartz; opx, orthopyroxene; cpx, clinopyroxene; amp calc, calculated amphibole composition (see the text); gl, average glass composition in primary silicate melt inclusions.

Fractionation of amphibole would produce compositional variations similar to those seen in opx-hosted MI (Fig. 8). The composition of primary MI trapped in cpx is consistent with qz + opx crystallization that followed amp fractionation (Fig. 8).

To test the effect of fractional crystallization on the trace element composition of the hybrid melt, various ratios of opx, cpx (with compositions determined in this study) and a hypothetical amp were added to the average MI composition to simulate a reverse fractional crystallization path. The trace element composition of the amp was estimated based on trace element partition coefficients between cpx and amp determined for peridotites by Ionov *et al.* (1997).

Addition of opx does not change the MI trace element patterns; however, all trace element concentrations decrease with increasing opx incorporation (Fig. 9a). This means that opx fractionation alone did not control the trace element pattern of the hybrid melt. Amp addition, however, leads to a decrease in the strongly incompatible element concentrations, disappearance of the positive Pb anomaly, development of negative Hf, Zr and Ti anomalies, and an increase in HREE and compatible elements (Fig. 9b). Addition of cpx to the MI has an effect similar to amp; however, the negative Hf, Zr and Ti anomalies and the decrease in the strongly incompatible element

concentrations are more significant (Fig. 9c). The results of this 'reverse' fractional crystallization calculation suggest that opx, cpx and amp fractionation from the original hybrid melt might lead to (1) slight increase in strongly incompatible elements such as Cs, Rb, Th, U and Ba, (2) development of a positive Pb anomaly, (3) disappearance of the negative Hf, Zr and Ti anomalies, and (4) a decrease in Yb, Lu, Sc, V and Cr concentrations in the residual melt (Fig. 9d). Significant trace element compositional changes, however, are observed only if there is a high degree of fractionation of these minerals (above 50%) from the hybrid melt, which is not supported by the major element compositions (Fig. 8).

Although the exact ratios of the fractionating minerals cannot be determined, the results suggest that the composition of the slab melt did not change significantly as a result of peridotite dissolution (assimilation) and fractional crystallization (Fig. 9d). Thus, the negative high field strength element (HFSE) anomalies, which are partially seen in the MI, as well as the negative Sr anomaly, are characteristic of the slab melt and not an artefact of hybridization. This interpretation is in accordance with the results of Rapp *et al.* (1999), who experimentally studied (at 3–8 GPa) the behaviour of trace elements at the peridotite–silicate melt interface at high melt/wall rock ratios.

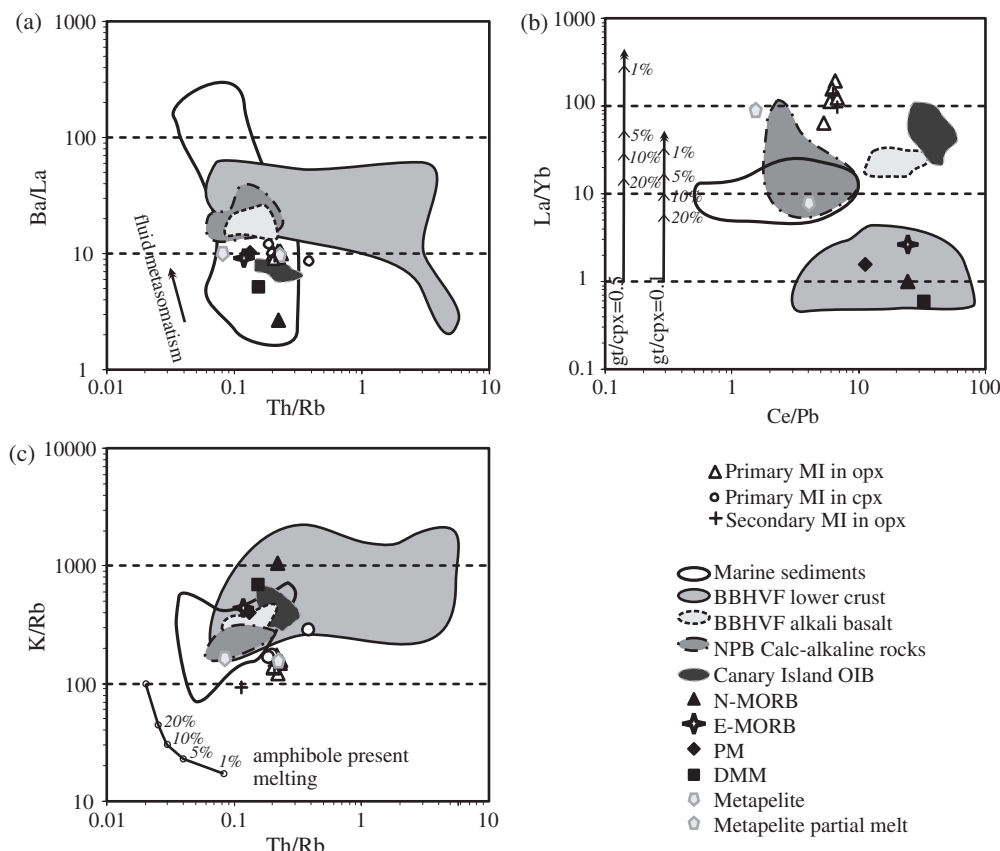


Fig. 10. Comparison of characteristic trace element ratios in the melt [represented by the melt inclusions (MI)] with the composition of different mantle sources [N-MORB (Hofmann, 1988), E-MORB (Sun & McDonough, 1989), primitive mantle (PM; McDonough & Sun, 1995), depleted MORB mantle (DMM; Salters & Stracke, 2004), Canary ocean island basalt (OIB; Praegel & Holm, 2006), subducted sediments (Plank & Langmuir, 1998), widespread volcanic rocks from the CPR (Embey-Isztin *et al.*, 1993; Harangi *et al.*, 2001), the local lower crust (known from granulite xenoliths; Embey-Isztin *et al.*, 2003) and metapelite rocks and their coexisting partial melts (Garcia-Casco *et al.*, 2001)]. The arrow in (a) shows the approximate effect of fluid metasomatism; the arrows in (b) show the effect of partial melting assuming various degrees of melting and garnet (gt) to clinopyroxene (cpx) ratio in the source [bulk partition coefficients were taken from Klemme *et al.*, (2002)]; (c) shows the effect of amphibole-present melting as a function of the degree of melting [batch partial melting and partition coefficients were taken from Xiong (2006)]. The results suggest that a low degree of partial melting of a garnet- and amphibole-bearing source is required to produce the observed melt compositions when considering melting of the most likely source components.

Slab melt generation, source components

The MI preserve the trace element pattern of the slab melt and MI compositions can be used to approximate the formation conditions of the melt. The low contents of HREE ($\text{La}_N/\text{Yb}_N = 85\text{--}134$) and Y (5.4–6.3 ppm) in the primary MI (Fig. 6) suggest the presence of garnet (gt) in the source (e.g. Nicholls & Harris, 1980). The low Nb and Ta concentrations, coupled with the negative Hf, Zr and Ti anomalies in the hybrid melt (Fig. 9d), imply rutile (ru) in the source (e.g. Green & Pearson, 1987). Garnet and rutile are typical constituents of both metabasalts and metasediments in subducted oceanic crust. Several features of the trace element composition of the MI (Fig. 6) resemble those of adakites (Fig. 6d), which have been interpreted as products of eclogite melting (Kay, 1978). However, the low Sr content of the MI

(74–116 ppm) and high K/Na ratios, and large ion lithophile element (LILE) and LREE concentrations, are not typical for adakites (>400 ppm Sr) (Fig. 6d). These features suggest that another phase that retains Sr may have been present in the source during slab melt generation and also that the source may have been enriched in incompatible trace elements and/or the degree of partial melting was small.

Ratios of incompatible elements with similar bulk partition coefficients can be used to obtain information on the composition of the source, as these are neither dependent on the degree of partial melting nor modified by crystallization processes. As such, we used Th/Rb, K/Rb, Ba/La and Ce/Pb ratios to distinguish different source components. Characteristic ratios in the MI (Table 2) are shown in Fig. 10. Ba/La ratios plot close to primitive mantle (PM)

and mid-ocean ridge basalt (MORB) values (Fig. 10a), suggesting that the melt was produced by melting of an eclogite with a normal (N)-MORB or enriched (E)-MORB composition. On the other hand, the Th/Rb, Ce/Pb and K/Rb ratios of the MI plot away from both MORB and PM. As K is significantly more compatible in amphibole compared with Rb, the presence of amphibole in the source is the most likely explanation for the low K/Rb ratios. Similarly, the Th/Rb ratio can also be shifted by melting in the presence of amphibole (Fig. 10c). The Ce/Pb ratio suggests involvement of another component, probably subducted sediment. The high La/Yb ratios can be produced by melting eclogite with a MORB composition only with a low degree of partial melting ($\leq 3\%$) (Fig. 10b). A higher degree of melting is possible (up to 20%) if a sedimentary component is also involved, because it is characterized by an elevated La/Yb ratio (Fig. 10b). These observations, combined with the high K/Na ratios, suggest a significant contribution of melt released from subducted metasediments.

High-pressure and -temperature experiments suggest that during melting of a metabasaltic slab at relatively high temperature and low pressure (~ 950 – 1000°C and below 2.0 GPa), plagioclase (pl) is stable in the residuum with gt, cpx and amp (Springer & Seck, 1997). The experimental results of Xiong *et al.* (2005), however, suggested that ru is a stable phase in subducted hydrated basalts only at pressures above 1.5 GPa (Fig. 11). Thus, to produce a silicate melt depleted in both Sr and HFSE, slab melting must have occurred at 1.5–2.0 GPa and a temperature below 1050°C . This is supported by the model partial melting calculations of Xiong (2006), which showed that silicate melts produced by low degrees of partial melting of a ru-bearing amp-eclogite at 2 GPa, 1050°C are strongly enriched in LILE and LREE and depleted in HREE, and show negative anomalies for Nb and Ta. A negative Sr anomaly appears only when pl occurs in significant amounts in the residue (Fig. 6f). Metapelite melting over a similar P – T range (~ 1.5 GPa, $>900^\circ\text{C}$) might leave behind a gt + cpx + opx (+ pl) + qz resitite (e.g. Patiño-Douce & Beard, 1995). In addition to plagioclase, apatite is a possible Sr sink in the source as it is stable over a wide P – T range in metabasaltic and metasedimentary rocks. One could argue that melt compositions similar to the MI could be produced by melting of garnet-bearing lower crustal granulites. However, the high Cr and Ni concentrations in pyroxenes in the studied xenolith provide strong evidence for a mantle origin (Fig. 6b, Table 2) as does the high Al(VI)/Al(IV) ratio (~ 2.4) in the clinopyroxene. Furthermore, the composition of the local lower crust inferred from granulite xenoliths of metagneous and metasedimentary origin (Embey-Isztin *et al.*, 2003) does not have high enough LREE enrichment to produce the very high La/Yb ratios observed (Fig. 6a).

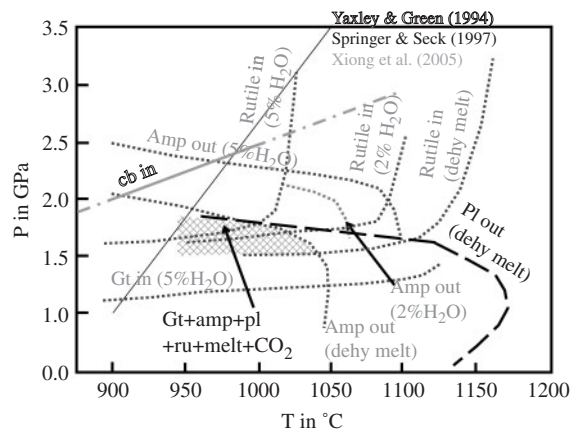


Fig. 11. Phase relations for hydrous metabasalts. Continuous line indicates the steady-state P – T path of a young and hot subducting oceanic plate (0 Myr old; subduction rate is 3 cm/year) (Peacock *et al.*, 1994). The diagram is compiled from the experimental data of Yaxley & Green (1994), Springer & Seck (1997) and Xiong *et al.* (2005). No rutile was found in the run products of Springer & Seck (1997) and plagioclase was absent from the run products of Xiong *et al.* (2005), but this may be the result of compositional differences in the starting materials, as TiO_2 and K_2O contents significantly affect rutile stability (Xiong *et al.*, 2005). The starting material used by Springer & Seck (1997) contained much less TiO_2 and K_2O , but higher CaO compared with that of Xiong *et al.* (2005). The cross-hatched field indicates the most probable pressure and temperature range for extraction of the studied silicate melt from an oceanic slab. amp, amphibole; pl, plagioclase; gt, garnet; ru, rutile; cb, carbonate;dehy melt, dehydration melting.

Crystallization conditions of the studied xenolith ($\sim 960^\circ\text{C}$ and >1.1 GPa) are close to those suggested for release of silicic melt from a subducted slab (Fig. 11). This implies that the slab-derived silicic melt did not migrate far from its source before it crystallized and trapped MI in cpx and opx.

We conclude that the studied qz-bearing opx-rich websterite was formed by reaction of a slab-derived siliceous melt with a mantle peridotite. Although we cannot estimate the initial composition of the slab melt with a high degree of accuracy, the trace element pattern and the volatile content of the MI suggest that melt generation occurred at a relatively shallow depth in the presence of garnet, amphibole, rutile and probably plagioclase in the residuum. The source composition cannot be unequivocally determined; however, major and trace element ratios indicate the probable involvement of a metasedimentary component.

The origin of secondary MI and interstitial silicate glass

The secondary MI are late-stage inclusions trapped in healed fractures in opx and cpx. Secondary MI-1 have compositions that are similar to the primary MI (Figs 5 and 6), although the fluid/melt ratio in secondary

MI is much more variable than in primary MI (Fig. 2). This suggests that secondary MI-1 were trapped from a melt compositionally similar to that which formed the primary inclusions, precluding the infiltration of host basalt along healed fractures during uplift. It also suggests that the source of secondary MI is the same as that of the primary MI, and possibly that the source may be the primary MI themselves. After solidification of the websterite, which contained large primary MI, the mantle experienced lower-pressure conditions, which might have led to decrepitation of the largest MI and then heterogeneous closure of the released melt in secondary MI. The inferred decrease in pressure might have been associated with the formation of the Pannonian Basin during the Miocene.

Interstitial silicate glass shows a wider compositional range than was observed for the primary and secondary MI-1 (Fig. 4, Table 1). Highly siliceous glass was found between qz and opx, whereas the glass between opx and cpx is poorer in SiO₂ and richer in other major elements. Thus, the composition of the interstitial glass was probably controlled by the surrounding mineral phases (opx + qz and cpx + opx, respectively). Basalt infiltration did not play a significant role in affecting the chemistry of the interstitial glass. Thus, we attribute the formation of the interstitial melt to an *'in situ'* melting episode that occurred during uplift in the host basaltic magma. Secondary MI-2 might have been trapped from these melts.

CONCLUSIONS

Mineralogical, textural and compositional data presented here provide convincing evidence that quartz-bearing opx-rich rocks can be formed in the upper mantle. The observed mineral assemblage crystallized from a hybrid melt developed at the interface between peridotite and SiO₂-rich silicate melt at about 960°C and pressure in excess of 1.1 GPa. The SiO₂-rich melt represents a partial melt from a subducted slab of oceanic lithosphere. The melt was released from the subducted slab at ~1.5–2.0 GPa and <1000°C, leaving behind a restite of cpx + amp + gt + pl/ap(?) + ru. The trace element composition of MI in both opx and cpx suggests the involvement of a metasedimentary component during slab melting. Melt inclusions in the studied xenolith provide direct evidence for the presence, migration and evolution of slab-derived SiO₂-rich melts in the sub-continental lithospheric mantle. The results of this study also support the notion that metasomatized mantle can be transported by tectonic processes and rotations to place subduction-related rocks great distances from areas where subduction was known to have occurred (see Kovács & Szabó, 2007; Kovács *et al.*, 2007). Kovács & Szabó (2007) and Kovács *et al.* (2007) concluded that the subduction enrichment of the ALCAPA lithosphere may have occurred before the Miocene along the Budva–Pindos subduction zone, which

is also a likely location for the formation of the qz-bearing orthopyroxene-rich websterite xenolith reported here.

ACKNOWLEDGEMENTS

The authors thank the members of Lithosphere Fluid Research Lab and Professor David Green (RSES, ANU) for fruitful discussions. The authors owe thanks to Professor M. Wilson, Professor Hilary Downes (Birkbeck College), Dr James Beard and an anonymous reviewer for their useful suggestions on an earlier version of this paper. This work was supported by OTKA K61182 and OTKA T043686 grants to K.T. and C.S. and by the Hungarian–American TET (Science & Technology Foundation) 17/MO/01 to C.S. This is Publication 28 in the series from the Lithosphere Fluid Research Lab at Eötvös University, Budapest.

REFERENCES

- Arai, S., Shimizu, Y. & Gervilla, F. (2003). Quartz diorite veins in a peridotite xenolith from Tallante, Spain: implications for reaction and survival of slab-derived SiO₂-oversaturated melt in the upper mantle. *Proceedings of The Japan Academy Series B—Physical And Biological Sciences* **79**, 145–150.
- Bali, E., Szabó, C., Vaselli, O. & Török, K. (2002). Significance of silicate melt pockets in upper mantle xenoliths from the Bakony–Balaton Highland Volcanic Field, Western Hungary. *Lithos* **61**, 79–102.
- Bali, E., Szabó, C., Peate, D. W., Falus, Gy., Hidas, K., Török, K. & Ntaflou, T. (2007). Remnants of boninitic melts in the upper mantle beneath the central Pannonian Basin?—The significance of orthopyroxene-rich websterite veins in peridotite xenoliths. *Mineralogy and Petrology* **90**, 51–72.
- Bali, E., Zanetti, A., Szabó, Cs., Peate, D. & Waight, T. E. (2008). Evolution of the subcontinental lithospheric mantle beneath the Central Pannonian Basin: trace element evidence from silicate melt pockets in mantle xenoliths from the Bakony–Balaton Highland Volcanic Field, (western Hungary). *Contributions to Mineralogy and Petrology* **155**, 165–179.
- Balogh, K., Árvai-Sós, E., Pécskay, Z. & Ravasz-Baranyi, L. (1986). K/Ar dating of post-Sarmatian alkali basaltic rocks in Hungary. *Acta Mineralogica Petrographica* **28**, 75–93.
- Benedek, K., Pécskay, Z., Szabó, Cs., Németh, T. & Jósvali, J. (2004). Paleogene igneous rocks in the Zala basin: link to the Paleogene magmatic activity along the Periadric lineament. *Geologica Carpathica* **55**, 43–50.
- Berkesi, M., Hidas, K. & Szabó, C. (2007). Reconstruction of fossil geotherm of the upper mantle beneath the Bakony–Balaton Highland Volcanic Field based on CO₂-fluid inclusions hosted in peridotite xenoliths from Tihany. *Hungarian Geophysics* **48**, 31–37 (in Hungarian with English abstract).
- Bianchini, G., Beccaluva, L., Bonadiman, C., Siena, F. & Vaccaro, C. (2004). Subduction and continental crust recycling—petrological evidence in mantle xenoliths from the Betic area (Spain). In: *32nd International Geophysical Conference, Florence*, p. 1150.
- Bodnar, R. J. (2003a). Introduction to fluid inclusions. In: Samson, I., Anderson, A. & Marshall, D. (eds) *Fluid Inclusions: Analysis and Interpretation*. Quebec: Mineralogical Association of Canada, pp. 1–8.

- Bodnar, R. J. (2003b). Re-equilibration of fluid inclusions. In: Samson, I., Anderson, A. & Marshall, D. (eds) *Fluid Inclusions: Analysis and Interpretation*. Quebec: Mineralogical Association of Canada, pp. 213–230.
- Bodnar, R. J. & Student, J. J. (2006). Melt inclusions in plutonic rocks: Petrography and microthermometry. In: Webster, J. D. (ed.) *Melt Inclusions in Plutonic Rocks*. Quebec: Mineralogical Association of Canada, pp. 1–26.
- Csontos, L. & Vörös, A. (2004). Mesozoic plate tectonic reconstruction of the Carpathian region. *Palaeogeography, Palaeoclimatology, Palaeoecology* **210**, 1–56.
- Cvetkovic, V., Downes, H., Prelevic, D., Jovanovic, M. & Lazarov, M. (2004). Characteristics of the lithospheric mantle beneath East Serbia inferred from ultramafic xenoliths in Palaeogene basanites. *Contributions to Mineralogy and Petrology* **148**, 335–357.
- Darling, R. S., Chou, I.-M. & Bodnar, R. J. (1997). An occurrence of metastable cristobalite in high pressure garnet granulite. *Science* **276**, 91–93.
- Danyushevsky, L. V., Della-Pasqua, F. N. & Sokolov S. (2000). Re-equilibration of melt inclusions trapped by magnesian olivine phenocrysts from subduction-related magmas: petrological implications. *Contributions to Mineralogy and Petrology* **138**, 68–83.
- Dobosi, G. (2003). *The geochemistry of upper mantle and lower crust based on the xenoliths of alkaline basalts from the Carpathian–Pannonian region*. Budapest: Hungarian Academy of Sciences.
- Dobosi, G., Downes, H., Embey-Isztin, A. & Jenner, G. A. (2003a). Origin of megacrysts and pyroxenite xenoliths from the Pliocene alkali basalts of the Pannonian Basin (Hungary). *Neues Jahrbuch für Mineralogie, Abhandlungen* **178**, 217–237.
- Dobosi, G., Kempton, P. D., Downes, H., Embey-Isztin, A., Thirlwall, M. & Greenwood, P. (2003b). Lower crustal granulite xenoliths from the Pannonian Basin, Hungary, Part 2: Sr–Nd–Pb–Hf and O isotope evidence for formation of continental lower crust by tectonic emplacement of oceanic crust. *Contributions to Mineralogy and Petrology* **144**, 671–683.
- Downes, H., Embey-Isztin, A. & Thirlwall, M. F. (1992). Petrology and geochemistry of spinel peridotite xenoliths from the western Pannonian Basin (Hungary)—evidence for an association between enrichment and texture in the upper mantle. *Contributions to Mineralogy and Petrology* **109**, 340–354.
- Embey-Isztin, A. (1976). Amphibolite/lherzolite composite xenolith from Szigliget, north of the Lake Balaton, Hungary. *Earth and Planetary Science Letters* **31**, 297–304.
- Embey-Isztin, A., Scharbert, H. G., Dietrich, H. & Poudrits, H. (1989). Petrology and geochemistry of peridotite xenoliths in alkali basalts from the Transdanubian volcanic region. *Journal of Petrology* **34**, 317–343.
- Embey-Isztin, A., Downes, H., James, D. E., Upton, B. G. J., Dobosi, G., Ingram, G. A., Harmon, R. S. & Scharbert, H. G. (1993). The petrogenesis of Pliocene alkaline volcanic rocks from the Pannonian Basin, eastern Central Europe. *Journal of Petrology* **34**, 317–343.
- Embey-Isztin, A., Dobosi, G., Altherr, R. & Meyer, H. P. (2001). Thermal evolution of the lithosphere beneath the western Pannonian Basin: evidence from deep-seated xenoliths. *Tectonophysics* **331**, 285–306.
- Embey-Isztin, A., Downes, H. & Kempton, P. D. (2003). Lower crustal granulite xenoliths from the Pannonian Basin, Hungary. Part 1: mineral chemistry, thermobarometry and petrology. *Contributions to Mineralogy and Petrology* **144**, 652–670.
- Falloon, T. J., Green, D. H., O'Neill, H. St. C. & Hibberson, W. O. (1997). Experimental test of low degree peridotite partial melt compositions: implications for the nature of anhydrous near-solidus peridotite melts at 1 GPa. *Earth and Planetary Science Letters* **152**, 149–162.
- Fodor, L., Csontos, L., Bada, G., Györfy, L. & Benkovics, L. (1999). Tertiary tectonic evolution of the Pannonian Basin and neighbouring orogens: a new synthesis of paleostress data. In: Durand, B., Jolivet, L., Horvath, F. & Seranne, M. (eds) *The Mediterranean Basins: Tertiary Extension within the Alpine Orogen*. Geological Society, London, *Special Publications* **156**, 295–334.
- Frezzotti, M. L. (2001). Silicate-melt inclusions study in magmatic rocks: applications to petrology. *Lithos* **55**, 273–299.
- Gaetani, G. A. & Grove, T. L. (1998). The influence of water on melting of mantle peridotite. *Contributions to Mineralogy and Petrology* **131**, 323–346.
- Garcia-Casco, A., Torres-Roldan, R. L., Millan, G., Monie, P. & Haissen, F. (2001). High-grade metamorphism and hydrous melting of metapelites in the Pinos terrane (W Cuba): Evidence for crustal thickening and extension in the northern Caribbean collisional belt. *Journal of Metamorphic Geology* **19**, 699–715.
- Green, T. H. & Pearson, N. J. (1987). An experimental study of Nb and Ta partitioning between Ti-rich minerals and silicate liquids at high pressure and temperature. *Geochimica et Cosmochimica Acta* **51**, 55–62.
- Halter, W. E., Pettke, T., Heinrich, C. A. & Rothen-Rutishauser, B. (2002). Major to trace element analysis of melt inclusions by laser-ablation ICP-MS: methods of quantification. *Chemical Geology* **183**, 63–86.
- Harangi, Sz., Downes, H., Kósa, L., Szabó, Cs., Thirlwall, M. F., Mason, P. R. D., & Matthey, D. (2001). Almandine garnet in calc-alkaline volcanic rocks of the Northern Pannonian Basin (Eastern-Central Europe): geochemistry, petrogenesis and geodynamic implications. *Journal of Petrology* **42**, 1813–1843.
- Heinrich, C. A., Pettke, T. *et al.* (2003). Quantitative multi-element analysis of minerals, fluid and melt inclusions by laser-ablation inductively-coupled-plasma mass-spectrometry. *Geochimica et Cosmochimica Acta* **67**, 3473–3497.
- Hermann, J. & Green, D. H. (2001). Experimental constraints on high pressure melting in subducted crust. *Earth and Planetary Science Letters* **188**, 149–168.
- Hirose, T., Kuniaki, K., Okuno, M., Fujinami, S. & Shinoda, K. (2005). X-ray, DTA and Raman studies of monoclinic tridymite and its higher temperature orthorhombic modification with varying temperature. *Journal of Mineralogical and Petrological Sciences* **100**, 55–69.
- Hofmann, A. W. (1988). Chemical differentiation of the Earth—the relationship between mantle, continental crust, and oceanic crust. *Earth and Planetary Science Letters* **90**, 297–314.
- Ionov, D. A., Griffin, W. L. & O'Reilly, S. Y. (1997). Volatile-bearing minerals and lithophile trace elements in the upper mantle. *Chemical Geology* **141**, 153–184.
- Kawakami, Y., Yamamoto, J. & Kagi, H. (2003). Micro-Raman densimeter for CO₂ inclusions in mantle-derived minerals. *Applied Spectroscopy* **57**, 1333–1339.
- Kay, R. W. (1978). Aleutian magnesian andesites—melts from subducted Pacific Ocean crust. *Journal of Volcanology and Geothermal Research* **4**, 117–132.
- Kázmér, M. & Kovács, S. (1985). Permian–Paleogene paleogeography along the eastern part of the Insubric–Periadriatic Lineament system: evidence for continental escape of the Bakony–Drauzug Unit. *Acta Geologica Hungarica* **28**, 71–84.
- Kinzler, R. J. & Grove, T. L. (1992). Primary magmas of mid-ocean ridge basalts 1. Experiments and Methods. *Journal of Geophysical Research* **97**, 6885–6906.
- Klemme, S., Blundy, J. D. & Wood, B. J. (2002). Experimental constraints on major and trace element partitioning during partial melting of eclogite. *Geochimica et Cosmochimica Acta* **66**, 3109–3123.

- Kovács, I. & Szabó, Cs. (2008). Middle Miocene volcanism in the vicinity of the Middle Hungarian Line: evidence for an inherited enriched mantle source: a review. *Journal of Geodynamics* **45**, 1–17.
- Kovács, I., Csontos, L., Szabó, Cs., Bali, E., Falus, G., Benedek, K. & Zajacz, Z. (2007). Paleogene–early Miocene igneous rocks and geodynamics of the Alpine–Carpathian–Pannonian–Danubian region: an integrated approach. In: Beccaluva, L., Bianchini, G. & Wilson, M. (eds) *Cenozoic Volcanism in the Mediterranean Area. Geological Society of America, Special Papers*, **418**, 93–112.
- Kushiro, I. (1969). The system forsterite–diopside–silica with and without water at high pressures. *American Journal of Science* **267A**, 269–294.
- Lenkey, L. (1999). Geotherms of the Pannonian Basin and its bearing on the tectonics of basin evolution. PhD thesis, Vrije Universiteit Amsterdam.
- Mader, U. K. & Berman, R. G. (1991). An equation of state for carbon dioxide to high pressure and temperature. *American Mineralogist* **76**, 1547–1559.
- Martin, U. & Németh, K. (2004). Mio/Pliocene phreatomagmatic volcanism in the Bakony–Balaton Highland Volcanic Field, Hungary. *Geologica Hungarica, Series Geologica* **26**, 73–132.
- McDonough, W. F. & Sun, S. S. (1995). The composition of the Earth. *Chemical Geology* **120**, 223–253.
- McInnes, B. I. A., Gregoire, M., Binns, R. A., Herzig, P. M. & Hannington, M. D. (2001). Hydrous metasomatism of oceanic subarc mantle, Lihir, Papua New Guinea: petrology and geochemistry of fluid-metasomatised mantle wedge xenoliths. *Earth and Planetary Science Letters* **188**, 169–183.
- Melcher, F., Meisel, T., Puhl, J. & Koller, F. (2002). Petrogenesis and geotectonic setting of ultramafic rocks in the Eastern Alps: constraints from geochemistry. *Lithos* **65**, 69–112.
- Morgan, Z. & Liang, Y. (2005). An experimental study of the kinetics of ilherzolite reactive dissolution with applications to melt channel formation. *Contributions to Mineralogy and Petrology* **150**, 369–385.
- Neumann, E. R. & Wulff-Pedersen, E. (1997). The origin of highly silicic glass in mantle xenoliths from the Canary Islands. *Journal of Petrology* **38**, 1513–1539.
- Nicholls, I. A. & Harris, K. L. (1980). Experimental rare-earth element partition-coefficients for garnet, clinopyroxene and amphibole coexisting with andesitic and basaltic liquids. *Geochimica et Cosmochimica Acta* **44**, 287–308.
- Parkinson, I. J. & Pearce, J. A. (1998). Peridotites from the Izu–Bonin–Mariana forearc (ODP leg 125): Evidence for mantle melting and melt–mantle interaction in a supra-subduction zone setting. *Journal of Petrology* **39**, 1577–1618.
- Patiño-Douce, A. E. & Beard, J. S. (1995). Dehydration-melting of biotite gneiss and quartz amphibolite from 3 to 15 kbar. *Journal of Petrology* **36**, 707–738.
- Peacock, S. M., Rushmer, T. & Thompson, A. B. (1994). Partial melting of subducting oceanic crust. *Earth and Planetary Science Letters* **121**, 227–244.
- Plank, T. & Langmuir, C. H. (1998). The chemical composition of subducting sediment and its consequences for the crust and mantle. *Chemical Geology* **145**, 325–394.
- Praegel, N. O. & Holm, P. M. (2006). Lithospheric contributions to high-MgO basanites from the Cumbre Vieja Volcano, La Palma, Canary Islands and evidence for temporal variation in plume influence. *Journal of Volcanology and Geothermal Research* **149**, 213–239.
- Prouteau, G., Maury, R. C., Sajona, F. G., Cotton, J. & Cotton, J. L. (2000). Behavior of niobium, tantalum and other high field strength elements in adakites and related lavas from the Philippines. *Island Arc* **9**, 487–498.
- Putirka, K., Mikaelian, H., Ryerson, F. J. & Shaw, H. (2003). New clinopyroxene–liquid thermobarometers for mafic, evolved and volatile-bearing lava compositions, with applications to lavas from Tibet and the Snake River Plain, ID. *American Mineralogist* **88**, 1542–1554.
- Rapp, R. P. & Watson, E. B. (1995). Dehydration melting of metabasalt at 8–32 kbar—implications for continental growth and crust–mantle recycling. *Journal of Petrology* **36**, 891–931.
- Rapp, R. P., Shimizu, N., Norman, M. D. & Applegate, G. S. (1999). Reaction between slab-derived melts and peridotite in the mantle wedge: experimental constraints at 3–8 GPa. *Chemical Geology* **160**, 335–356.
- Sajona, F. G., Maury, R. C., Pubellier, M., Leterrier, J., Bellon, H. & Cotton, J. (2000). Magmatic source enrichment by slab-derived melts in a young post-collision setting, central Mindanao (Philippines). *Lithos* **54**, 173–206.
- Salter, V. J. M. & Stracke, A. (2004). Composition of the depleted mantle. *Geochemistry, Geophysics, Geosystems* **5**, doi: 10.1029/2003GC000597.
- Santos, J. F., Schärer, U., Ibaguchi, J. I. G. & Girardeau, J. (2002). Genesis of pyroxenite-rich peridotite at Cabo Ortegal (NW Spain): Geochemical and Pb–Sr–Nd isotope data. *Journal of Petrology* **43**, 17–43.
- Shimizu, Y., Arai, S., Morishita, T., Yurimoto, H. & Gervilla, F. (2004). Petrochemical characteristics of felsic veins in mantle xenoliths from Tallante (SE Spain): an insight into activity of silicic melt within the mantle wedge. *Transactions of the Royal Society of Edinburgh: Earth Sciences* **95**, 265–276.
- Skjerlie, K. P. & Patiño-Douce, A. E. (2002). The fluid-absent partial melting of a zoisite-bearing quartz eclogite from 1.0 to 3.2 GPa: Implications for melting in thickened continental crust and for subduction-zone processes. *Journal of Petrology* **43**, 291–314.
- Springer, W. & Seck, H. A. (1997). Partial fusion of basic granulites at 5 to 15 kbar: Implications for the origin of TTG magmas. *Contributions to Mineralogy and Petrology* **127**, 30–45.
- Student, J. J. & Bodnar, R. J. (1999). Synthetic fluid inclusions XIV: Microthermometric and compositional analysis of coexisting silicate melt and aqueous fluid inclusions trapped in the haplogranite–H₂O–NaCl–KCl system at 800°C and 2000 bars. *Journal of Petrology* **40**, 1509–1525.
- Student, J. J. & Bodnar, R. J. (2004). Silicate melt inclusions in porphyry copper deposits: Identification and homogenization behavior. *Canadian Mineralogist* **42**, 1563–1600.
- Szabó, C., Bodnar, R. J. & Sobolev, A. V. (1996). Metasomatism associated with subduction-related, volatile-rich silicate melt in the upper mantle beneath the Nograd–Gomor volcanic field, northern Hungary southern Slovakia: Evidence from silicate melt inclusions. *European Journal of Mineralogy* **8**, 881–899.
- Szabó, C., Falus, G., Zajacz, Z., Kovács, I. & Bali, E. (2004). Composition and evolution of lithosphere beneath the Carpathian–Pannonian Region: a review. *Tectonophysics* **393**, 119–137.
- Sun, S. S. & McDonough, W. F. (1989). Chemical and isotopic systematics of oceanic basalts: implications for mantle composition and processes. In: Saunders, A. D. & Norry, M. J. (eds) *Magmatism in the Ocean Basins. Geological Society, London, Special Publications* **42**, 315–345.
- Török, K. & De Vivo, B. (1995). Fluid inclusions in upper mantle xenoliths from the Balaton Highland, Western Hungary. *Acta Volcanologica* **7**, 277–284.
- Török, K., Bali, E., Szabó, C. & Szakál, J. A. (2003). Sr-barite droplets associated with sulfide blebs in clinopyroxene megacrysts

- from basaltic tuff (Szentbékallá, western Hungary). *Lithos* **66**, 275–289.
- Török, K., Dégi, J., Szép, A. & Marosi, G. (2005). Reduced carbonic fluids in mafic granulite xenoliths from the Bakony–Balaton Highland Volcanic Field, W-Hungary. *Chemical Geology* **223**, 93–108.
- Vaselli, O., Downes, H., Thirlwall, M. F., Vannucci, R. & Coradossi, N. (1996). Spinel-peridotite xenoliths from Kapfenstein (Graz Basin, Eastern Austria): A geochemical and petrological study. *Mineralogy and Petrology* **57**, 23–50.
- Viti C. & Frezzotti, M. L. (2000). Re-equilibration of glass and CO₂ inclusions in xenolith olivine: a TEM study. *American Mineralogist* **85**, 1390–1396.
- Vityk, M. O., Bodnar, R. J. & Doukhan, J.-C. (2000). Synthetic fluid inclusions: XV. TEM investigation of plastic flow associated with re-equilibration of synthetic fluid inclusions in natural quartz. *Contributions to Mineralogy and Petrology* **139**, 285–297.
- Wulff-Pedersen, E., Neumann, E. R. & Jensen, B. B. (1996). The upper mantle under La Palma, Canary Islands: formation of Si–K–Na-rich melt and its importance as a metasomatic agent. *Contributions to Mineralogy and Petrology* **125**, 113–139.
- Wulff-Pedersen, E., Neumann, E. R., Vannucci, R., Bottazzi, P. & Ottolini, L. (1999). Silicic melts produced by reaction between peridotite and infiltrating basaltic melts: ion probe data on glasses and minerals in veined xenoliths from La Palma, Canary Islands. *Contributions to Mineralogy and Petrology* **137**, 59–82.
- Xiong, X. L. (2006). Trace element evidence for growth of early continental crust by melting of rutile-bearing hydrous eclogite. *Geology* **34**, 945–948.
- Xiong, X. L., Adam, J. & Green, T. H. (2005). Rutile stability and rutile/melt HFSE partitioning during partial melting of hydrous basalt: Implications for TTG genesis. *Chemical Geology* **218**, 339–359.
- Yaxley, G. M. & Green, D. H. (1994). Experimental demonstration of refractory carbonate-bearing eclogite and siliceous melt in the subduction regime. *Earth and Planetary Science Letters* **128**, 313–325.
- Zajacz, Z., Halter, W. *et al.* (2005). A composition-independent quantitative determination of the water content in silicate glasses and silicate melt inclusions by confocal Raman spectroscopy. *Contributions to Mineralogy and Petrology* **150**, 631–642.



Deltech Furnaces

Sustained operating
temperatures to 1800°
Celsius

www.deltechfurnaces.com



Gas Mixing System



An ISO 9001:2015 certified company

Custom Vertical Tube



ASME NQA-1 2008 Nuclear Quality Assurance



Standard Vertical Tube



Control systems are certified by Intertek UL508A compliant

Bottom Loading Vertical Tube